# A FIRST-PRINCIPLES INVESTIGATION OF THE TRANSITION BETWEEN TWO- AND THREE-DIMENSIONAL THERMAL TRANSPORT IN GRAPHENE AND GRAPHITE

by

Patrick Strongman

Submitted in partial fulfillment of the requirements
for the degree of Master of Science

at

Dalhousie University
Halifax, Nova Scotia
December 2019

*This thesis is dedicated to Deanna Kerry.*

# Table of Contents

# List of Figures

## Abstract

Two-dimensional materials have become a popular research area over the past two decades because of their unique physical properties. The low dimensionality of these materials leads to interesting, and useful, transport properties such as thickness-dependent band gaps and high electrical and thermal conductivity. These materials have applications in nanoelectronics, optoelectronics, and thermoelectric energy generation, the performance of which depends sensitively on understanding and controlling how heat transport occurs.

Most low dimensional materials can be derived by isolating them from their bulk counterparts, which are often comprised of stacks of the two-dimensional layers that are weakly bound together. These layered bulk materials often maintain some of the two-dimensional characteristics of their monolayer form because of the weak interlayer bonds. One common example of such a quasi-2D material is graphite, which is made of layered carbon sheets, i.e. graphene. When going from graphite to graphene the room-temperature in-plane thermal conductivity varies from approx. 2000 $\mathrm{W\,m^{-1}\,K^{-1}}$ to 5800 $\mathrm{W\,m^{-1}\,K^{-1}}$, respectively. Both values are exceptionally high, but there is still a large difference between the two. Nevertheless, the majority of studies focus either on the bulk or low-dimensional versions of materials, with little focus on how the transition from 3D to 2D influences the microscopic properties and transport characteristics.

The purpose of this study was to explain how the thermal transport properties of layered materials transition between two and three dimensions. Graphene and graphite were used as simple materials to model this transition. The thermal transport properties were calculated from first-principles using density functional theory (DFT) and iterative solutions to the Boltzmann transport equation (BTE). The transition between two and three dimensions was modelled by systematically moving the layers of graphite apart from each other until they were essentially isolated graphene sheets.

The converged $\kappa$ values of the limiting cases of graphite and graphene agree with experimental measurements and previous calculations, with the stretched cases showing a monotonically increasing thermal conductivity from $\kappa_{\mathrm{graphite}}$ to $\kappa_{\mathrm{graphene}}$. Surprisingly, the largest variation in the thermal transport properties resulted from changes in the phonon dispersion. This is contrary to the previous belief that the difference in $\kappa$ resulted from certain three-phonon selection rules in graphene, which reduce the scattering probability, and do not apply to graphite. The selection rules appear to mostly still apply to graphite and the stretched graphite cases, indicating that the primary mechanism resulting in the differences between $\kappa_{\mathrm{graphene}}$ and $\kappa_{\mathrm{graphite}}$ was the shape of the phonon dispersion, and a corresponding shift in the phonon DOS. This type of analysis could be applied to other layered materials in the future to identify materials with the potential to be exceptional thermal conductors.

## List of Abbreviations and Symbols Used

| | |
|---|---|
| $C_{n,\boldsymbol{k},\boldsymbol{K}}$ | Coefficients for Bloch waves. |
| $D_{ij}^{\alpha\beta}(\boldsymbol{q})$ | The dynamical matrix. |
| $E_0$ | Ground state energy of a system in equilibrium. |
| $E_\lambda$ | Energy of phonon state $\lambda$. |
| $E_i^\alpha$ | Total energy when atom $i$ is displaced in the $\alpha$ direction. |
| $E_i$ | Energy of a Kohn-Sham orbital $\psi_i(\boldsymbol{r})$. |
| $E_{GS}$ | Electronic ground state energy. |
| $M_i$ | Mass of the $i$th atom. |
| $N_k$ | Number of electron wavevectors in the discretized BZ. |
| $N_q$ | Number of phonon wavevectors in the discretized BZ. |
| $N$ | Number of atoms in the primitive cell. |
| $T$ | Temperature. |
| $V_{\lambda\lambda'\lambda''}^{\pm}$ | Scattering matrix elements for three-phonon scattering. |
| $V_{KS}$ | Effective potential for solving the Kohn-Sham equations. |
| $W_\lambda^{\pm}$ | Weighted phase space for three-phonon scattering. |
| $\Delta r_i^\alpha$ | A small displacement of atom $i$ from equilibrium in direction $\alpha$. |
| $\Gamma_{\lambda\lambda'\lambda''}^{\pm}$ | Three-phonon scattering rates obtained from Fermi's golden rule. |
| $\Phi_0$ | Equilibrium lattice potential energy. |
| $\Phi$ | Lattice potential energy. |
| $\alpha\beta\gamma$ | Variables representing cartesian directions. |
| $\boldsymbol{F}_i$ | The force on atom $i$. |
| $\boldsymbol{K}$ | Reciprocal wavevector used in electronic wavefunctions. |
| $\boldsymbol{Q}$ | Reciprocal lattice vector used in phonon theory. |
| $\boldsymbol{R}$ | Lattice vector. |
| $\boldsymbol{\Delta}_\lambda$ | Linear correction term to the BTE. |
| $\boldsymbol{a}_1, \boldsymbol{a}_2, \boldsymbol{a}_3$ | Primitive lattice vectors. |
| $\boldsymbol{l}_\lambda$ | Coefficient used in the linear correction to the BTE. |
| $\boldsymbol{p}$ | Momentum. |

| | |
|---|---|
| $\boldsymbol{q}$ | Phonon wavevector. |
| $\boldsymbol{r}_i^0$ | Equilibrium position vector of atom $i$. |
| $\boldsymbol{r}$ | Position vector. |
| $\boldsymbol{u}_i$ | Small atomic displacement from equilibrium. |
| $\ddot{u}_i^\alpha$ | Second time-derivative of atomic displacement of atom $i$. |
| $\epsilon_i^\alpha$ | Phonon polarization vector. |
| $\hat{T}$ | Kinetic energy operator. |
| $\hbar$ | Reduced Planck's constant. |
| $\kappa^{\alpha\beta}$ | Thermal conductivity tensor element. |
| $\kappa_e$ | Electronic contribution to thermal conductivity. |
| $\kappa_l$ | Lattice thermal conductivity. |
| $\kappa_{\text{cumulative}}$ | Electronic contribution to thermal conductivity. |
| $\lambda$ | Phonon state label. |
| $\nabla^\beta T$ | Temperature gradient. |
| $\omega$ | Angular frequency of a phonon mode. |
| $\psi_i(\boldsymbol{r})$ | Kohn-Sham orbital. |
| $\psi_{n,\boldsymbol{k}}(\boldsymbol{r})$ | Bloch wavefunction. |
| $\theta_x$ | Angle of phonon eigenvectors from the $x$ axis. |
| $\theta_z$ | Angle of phonon eigenvectors from the $z$ axis. |
| $\widetilde{\Phi}_{ij}^{\alpha\beta}(\boldsymbol{q})$ | Fourier transform of the second-order interatomic force constants. |
| $\xi_{\lambda\lambda'}$ | Ratio between the angular frequency $\omega_{\lambda'}$ and $\omega_\lambda$. |
| $a, b, c$ | Crystal coordinates. |
| $a$ | Lattice constant. |
| $c$ | Lattice constant. |
| $f^0$ | The Bose-Einstein distribution. |
| $f_\lambda$ | The distribution function for phonon state $\lambda$. |
| $ijk$ | Atomic indices. |
| $j^\alpha$ | Heat flux. |
| $k_B$ | Boltzmann's constant. |
| $m$ | Number of z components for a given IFC. |
| $n(\boldsymbol{r})$ | Electron density. |

| | |
|---|---|
| $p$ | Label for the phonon branch. |
| $t$ | Time. |
| $u_{n,\boldsymbol{k}}(\boldsymbol{r})$ | A function with the periodicity of the lattice. |
| $v_\lambda^\alpha$ | The speed in the $\alpha$ direction of a phonon in state $\lambda$. |
| $x, y, z$ | Cartesian directions. |
| BTE | Boltzmann transport equation. |
| BZ | Brillouin Zone. |
| DFPT | Density functional perturbation theory. |
| DFT | Density functional theory. |
| DOS | Density of states. |
| FD | Finite displacement. |
| GGA | Generalized gradient approximation. |
| IFC | Interatomic force constant. |
| LA | Longitudinal acoustic phonon modes. |
| LDA | Local density approximation. |
| LO' | Low-energy longitudinal optical phonon modes. |
| $MoS_2$ | Molybdenum disulfide. |
| PAW | Projector augmented wave. |
| PBE | Predew-Burke-Erzenhoff. |
| QE | Quantum Espresso. |
| QHA | Quasi-harmonic approximation. |
| TA | Transverse acoustic phonon modes. |
| TO' | Low-energy longitudinal optical phonon modes. |
| XDM | Exchange-hole dipole moment. |
| ZA | Flexural acoustic phonon modes. |
| ZO' | Low-energy longitudinal optical phonon modes. |

## Acknowledgements

I would first like to thank my supervisor Dr. Jesse Maassen for all of his guidance. His help was invaluable, and I truly enjoyed working on this project with him over the past two years. I would also like to thank the other members of our group: Cameron Rudderham, Fouad Kaadou, and Vahid Askarpour for all of their help and camaraderie, as well as the others who worked with us in room 207, or frequently visited.

I would like to thank some of my closest friends from back home on PEI: Ben Marchbank, Zach Graham, and Zak McLure, for keeping in touch and keeping me entertained when I would take a break.

I am very thankful for the financial support from NSERC, the Government of Nova Scotia, and Dalhousie University. Furthermore, I would like to acknowledge that this project would not have been possible without the computational resources supplied by Compute Canada.

Finally, thank you to my family. There are too many names to reasonably list here, but I appreciate all of your love and support.

# Chapter 1

# Introduction

The study of two-dimensional materials became the focus of many materials researchers in the past two decades [1–6] after the experimental isolation of graphene in 2004 [7]. Graphene is a single two-dimensional sheet of carbon atoms with exceptional physical properties. The strong bonds between carbon atoms makes it one of the strongest known materials. Its experimentally determined thermal conductivity at room temperature is higher than any other material [8], and it also has exceptionally mobile charge carriers [9].

Graphite is the bulk form of graphene. It is composed of layers of graphene that are stacked on top of each other and weakly bound. It is a member of a class of materials called layered materials. These materials are of special interest to materials researchers because the weak interlayer bonding often allows the bulk form of the material to retain some of the characteristics of a monolayer. The differences in strength between the in-plane and cross-plane bonds often also leads to highly anisotropic properties [10, 11].

While graphene has exceptional mechanical, thermal, and electronic properties, it has no band gap, which restricts the number of applications for which it may be useful. Methods have been developed to artifically create a bandgap in graphene, but they often lead to losses of the desireable thermal and electronic transport properties [12, 13]. Because of this, the focus of two-dimensional materials research in recent years has shifted from graphene to other 2D materials with interesting transport and chemical properties.

One class of layered materials with monolayers that possess particularly interesting properties are transition metal dichalcogenides [14–17]. These materials are composed of monolayers with a stoichiometry of $MX_2$, where M is a transition metal and X is from the chalcogen group. One commonly studied example is $MoS_2$. The bulk forms of these materials often maintain much of the two-dimensional characteristics

because of the weak bonds between layers. These materials exhibit a diverse range of useful, and sometimes exotic, properties. Their electronic transport properties vary between insulators, metals, and semiconductors, often with anisotropic transport characteristics [10, 11]. Slabs of these materials that are only a few monolayers thick display thickness-dependent properties, which can be tuned by varying the number of monolayers in the slab [18, 19]. The thickness dependent and anisotropic properties allow for a single material to be used for a variety of applications, simply by changing the thickness of a slab, or by changing the direction of transport.

While these materials exhibit interesting properties in both their bulk and monolayer form, it is not clear what mechanism leads to the differences in their thermal transport properties. Experiments on graphene have measured thermal conductivites of up to 5000 $\mathrm{W\,m^{-1}\,K^{-1}}$ [8]. Meanwhile, the in-plane thermal conductivity of graphite at room temperature is around 2000 $\mathrm{W\,m^{-1}\,K^{-1}}$, and the cross-plane thermal conductivity is around 7 $\mathrm{W\,m^{-1}\,K^{-1}}$ [20]. The in-plane thermal conductivity of graphite is still impressively large, but it is a significant reduction from that of graphene. This reduction in thermal conductivity is a common occurrence between monolayer and bulk materials [21]. Understanding the mechanism behind these differences may provide some insight on what generally leads to high or low thermal conductivites in these materials.

Discovering what the mechanism is requires an understanding of how the thermal transport properties evolve through a transition from a monolayer to a bulk material. In non-metals, such as graphene, heat is primarily transported by phonons, which are vibrations in the lattice. In order to calculate their contributions to the thermal conductivity of a material, the energy, velocity, and occupation of phonons in each state must be known. In recent years, with the increasing availability of software and computational resources, it has become commonplace to calculate these properties from first-principles. Density functional theory (DFT) is often used to calculate the phonon dispersion, which gives the phonon energies and velocities [22, 23]. Iterative solutions to the Boltzmann transport equation (BTE) [24] then provide the occupation number of each phonon state, along with the converged thermal conductivity and various phonon scattering properties.

Phonon scattering is an important factor for determining the occupation of phonon

modes. Three-phonon scattering is usually the dominant scattering process near room temperature that contributes to thermal resistance. The phonon energies, velocities, and scattering rates are all determined by the interatomic force constants (IFCs), which can be calculated using DFT.

In graphene, there are a set of selection rules that significantly reduces the probability of the scattering events of certain phonon modes. These selection rules depend on a mirror symmetry within the graphene plane, which maps every atom onto itself [25–27]. This mirror symmetry does not exist in few-layer graphene or bulk graphite, which will be illustrated next. In order to determine if this loss of selection rules is the main contributor to the reduced thermal conductivity of graphite, the thermal properties of graphene must be analysed through a transition from its bulk to monolayer form.

When studying the transition from 2D to 3D, a common approach is to begin with a monolayer, and systematically increase the number of layers until it is effectively bulk [27, 28]. This approach could be problematic for the transition from graphene to graphite since the mirror symmetry that the high thermal conductivity of graphene is thought to depend on is instantaneously broken by the addition of a second layer. For any even number of layers, there are no reflection planes. This is illustrated in Figure 1.1. For odd numbers of layers there would only a reflection plane on the central sheet. However, graphite contains a mirror symmetry plane within each graphene layer, so the few-layer form of the material may not be an accurate representation of graphite.

In order to address the breaking of symmetry in the transition, a different approach is used in the present study. Beginning with graphite, the structure is systematically 'stretched' in the cross-plane direction so as to slowly increase the interlayer separation. Eventually, the distance between layers is large enough that the system is effectively isolated graphene sheets. A visualization of this process is seen in Figure 1.2. While this stretching process is likely unstable and unphysical, it should serve as a useful model to see how the transition from 3D to 2D occurs for any layered materials, regarding their thermal properties. Also, by using this technique there should be a slow breaking of the selection rules when looking at the transition from graphene to graphite since the mirror symmetry will be preserved, as opposed to the

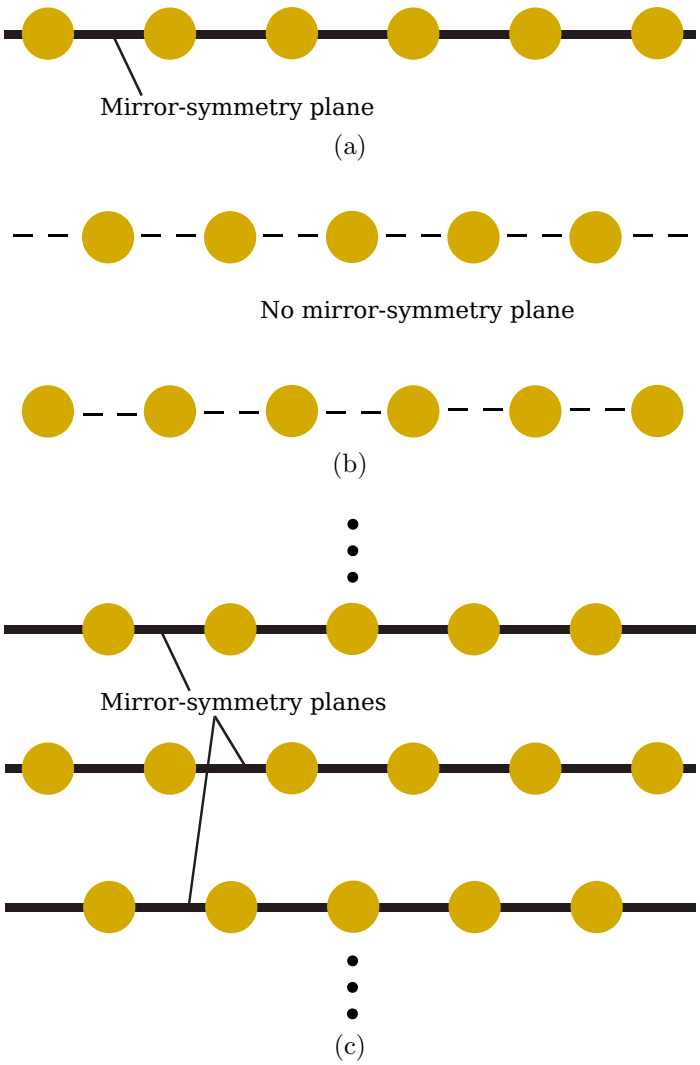


Figure 1.1: Diagram of the mirror symmetry planes in (a) graphene, (b) bilayer graphene, and (c) graphite. Each of the yellow circles are a carbon atom, and the solid black lines are mirror symmetry planes. Each layer of carbon atoms represents a whole graphene sheet.

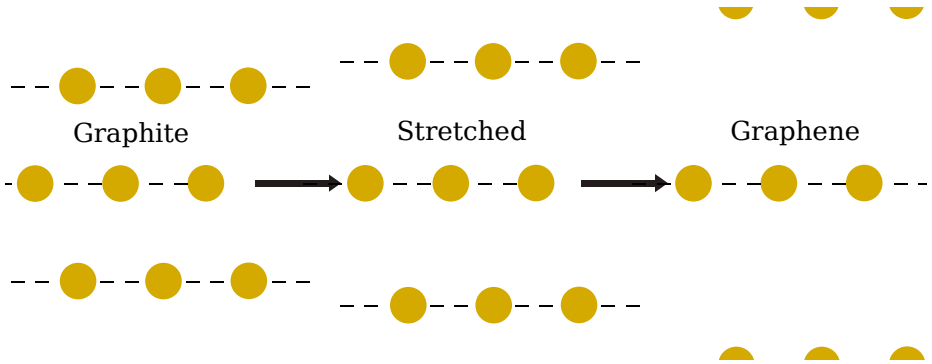


Figure 1.2: A visualization of the process of stretching graphite until it is effectively graphene. The yellow circles are the carbon atoms. The distance between graphene layers increases from left to right.

instantaneous breaking that occurs when going from monolayer to a bilayer graphene. If the breaking of selection rules is primarily responsible for the difference in thermal conductivity, then a significant difference in the IFCs that lead to the selection rules should be observed through this transition.

In this thesis, DFT was used to calculate the interatomic force constants for each case between graphite and graphene. The IFCs were then used to calculate the phonon properties, and to solve the BTE to obtain a thermal conductivity for each interlayer separation. A variety of factors that affect the thermal conductivity were analyzed, such as the phonon dispersion, three-phonon scattering rates, cumulative thermal conductivities, etc. By analyzing how every important thermal property changes during the transition from 3D to 2D, it should be possible to isolate the primary mechanism, or mechanisms, that contribute to differences in the thermal conductivity. Graphene and graphite were used in this case because of their relatively simple structures, but the general results that were obtained should be applicable to other layered materials.

The following chapters will begin with an explanation of the theory of phonon transport, followed by the computational techniques that were used to calculate the thermal transport properties. The next chapter presents the results obtained for each of the cases, beginning with the limiting cases of graphene and graphite, followed by the stretched graphite cases. The analysis of the results leads to the conclusion that the differences in the thermal conductivity of graphene and graphite are primarily the result of changes in the shape of the phonon dispersion, which provides graphene with

more phonons with higher velocities for transport than graphite, and not necessarily the loss of selection rules. This result is significant since the changes in phonon dispersion should manifest in a similar way in other layered materials. Therefore, this type of analysis could potentially be applied to layered materials in general, and could aid in identifying properties of layered materials that lead to high or low conductivites.

# Chapter 2

# Theory

Standard heat transport in solids can be described using Fourier's Law

$$j^{\alpha} = -\kappa^{\alpha\beta}\nabla^{\beta}T, \tag{2.1}$$

where the heat flux $j^{\alpha}$ is proportional to the temperature gradient $\nabla^{\beta}T$. The proportionality constant $\kappa^{\alpha\beta}$ is an element of the thermal conductivity tensor, and the greek superscripts, $\alpha, \beta$, represent the cartesian directions $x, y, z$. Equation 2.1 describes the amount of heat that travels through a unit area in the $\alpha$ direction, in units of $\mathrm{Wm}^{-2}$, resulting from a temperature gradient in the $\beta$ direction, in units of $\mathrm{K\,m}^{-1}$. The units of $\kappa$ are therefore $\mathrm{W\,m}^{-1}\,\mathrm{K}^{-1}$. Materials that conduct heat well have large conductivities, while thermal insulators have low conductivities.

The thermal conductivity can be broken up into two components:

$$\kappa = \kappa_e + \kappa_l. \tag{2.2}$$

Here, $\kappa_e$ is the thermal conductivity contribution from electrons, and $\kappa_l$ is the lattice thermal conductivity. The electronic contribution is a result of electrons that have excess kinetic energy carried with them as they travel through a material with a temperature gradient. The lattice thermal conductivity is from the vibrations of atoms in the lattice. Lattice vibrations are usually modelled as phonons, which are quasiparticles that represent the normal modes of vibration, and travel through the lattice carrying energy in the form of heat.

In metals, electrons are usually the dominant heat carrier since conduction electrons are abundant. Meanwhile, phonons tend to be the majority carriers in electric insulators and semiconductors since there are few mobile electrons. In the case of graphene and graphite, phonons carry nearly all of the heat in the system, so the electronic contribution will be omitted. The focus of this thesis is to study $\kappa_l$ and

how it changes with dimensionality.

## 2.1 Crystal Structure

Many solid materials are composed of periodic arrays of atoms arranged in a crystal structure. The crystal structure can be decomposed into a lattice and a basis: where the lattice is an infinite series of regularly repeating points generated by lattice vectors; and the basis describes the position of atoms around the lattice points [29, 30]. The primitive cell is defined by the primitive lattice vectors $\boldsymbol{a}_1, \boldsymbol{a}_2, \boldsymbol{a}_3$ which contain the smallest repeating series of atoms within the crystal. The lattice vectors $\boldsymbol{R}$ are then any vector that is a linear combination of the primitive lattice vectors

$$\boldsymbol{R} = n_1\boldsymbol{a}_1 + n_2\boldsymbol{a}_2 + n_3\boldsymbol{a}_3, \tag{2.3}$$

where $n_1, n_2, n_3$ are integers. Any point $\boldsymbol{r}'$ in the crystal is equivalent to any other point $\boldsymbol{r}$ provided they are separated by some lattice vector $\boldsymbol{R}$.

The positions of atoms within the primitive cell are usually written in terms of the primitive lattice vectors, or crystal coordinates. An atom positioned at $(a, b, c)$ in crystal coordinates is at $\boldsymbol{r} = a\boldsymbol{a}_1 + b\boldsymbol{a}_2 + c\boldsymbol{a}_3$.

Graphene has a two-dimensional hexagonal lattice structure, which is described by two primitive lattice vectors

$$\boldsymbol{a}_1 = a\hat{\boldsymbol{x}} \tag{2.4}$$

$$\boldsymbol{a}_2 = \frac{1}{2}a\hat{\boldsymbol{x}} + \frac{\sqrt{3}}{2}a\hat{\boldsymbol{y}}. \tag{2.5}$$

The vectors are each the same length, $a = 2.46$ Å, and the angle between the two is $60°$. There are two carbon atoms in each unit cell. In crystal coordinates, the first is arbitrarily placed at $(0, 0)$, and the second is at $(2/3, 2/3)$. The bonds between carbon atoms have a length of $a/\sqrt{3} \approx 1.42$ Å. An illustration of the atomic structure is shown in Figure 2.1

Graphite is composed of layers of graphene where each subsequent layer is shifted from the previous, resulting in an AB layering formation. The crystal structure for

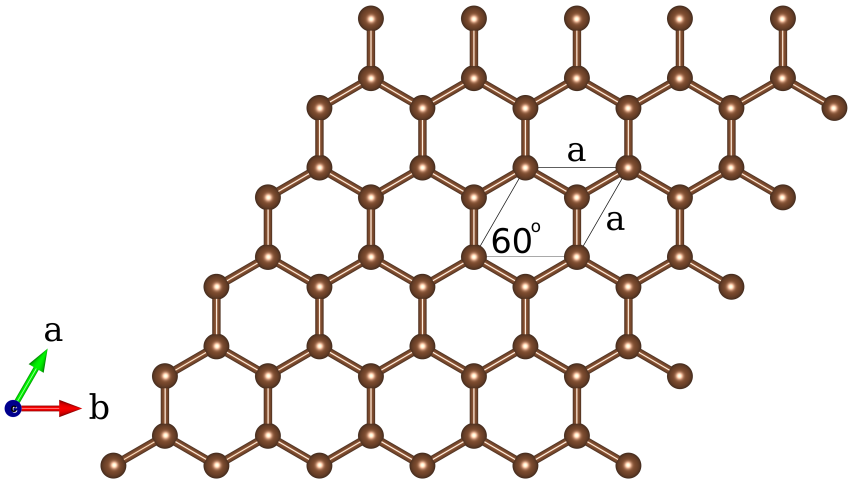


Figure 2.1: The atomic structure of graphene, generated by VESTA [31]. The distance between bonded carbon atoms is 1.42 Å, and $|a| = 2.46$Å [32].

graphite is a three-dimensional hexagonal lattice with primitive lattice vectors

$$\boldsymbol{a}_1 = a\hat{\boldsymbol{x}} \tag{2.6}$$

$$\boldsymbol{a}_2 = \frac{1}{2}a\hat{\boldsymbol{x}} + \frac{\sqrt{3}}{2}a\hat{\boldsymbol{y}} \tag{2.7}$$

$$\boldsymbol{a}_3 = c\hat{\boldsymbol{z}}. \tag{2.8}$$

Here, $c$ is the cross-plane lattice vector, with an experimental value of $c = 2.71a \approx 6.71$Å at room temperature [32]. There are four atoms in the primitive cell of graphite, which are positioned at $(0, 0, 0)$, $(2/3, 2/3, 0)$, $(1/3, 1/3, 1/2)$, and $(1, 1, 1/2)$ in crystal coordinates. The graphene layers have very strong bonding between atoms within a layer, but weak interlayer interactions dominated by Van der Waals forces; hence, there is a difference in bond lengths between carbon atoms in-plane and cross-plane.

The difference in bond strength leads to interesting properties, such as anisotropic transport. In graphite, the thermal conductivity in-plane is significantly larger than the cross-plane thermal conductivity because of the weak interaction between layers. Meanwhile, the in-plane thermal conductivity is comparable to that of a single graphene layer.

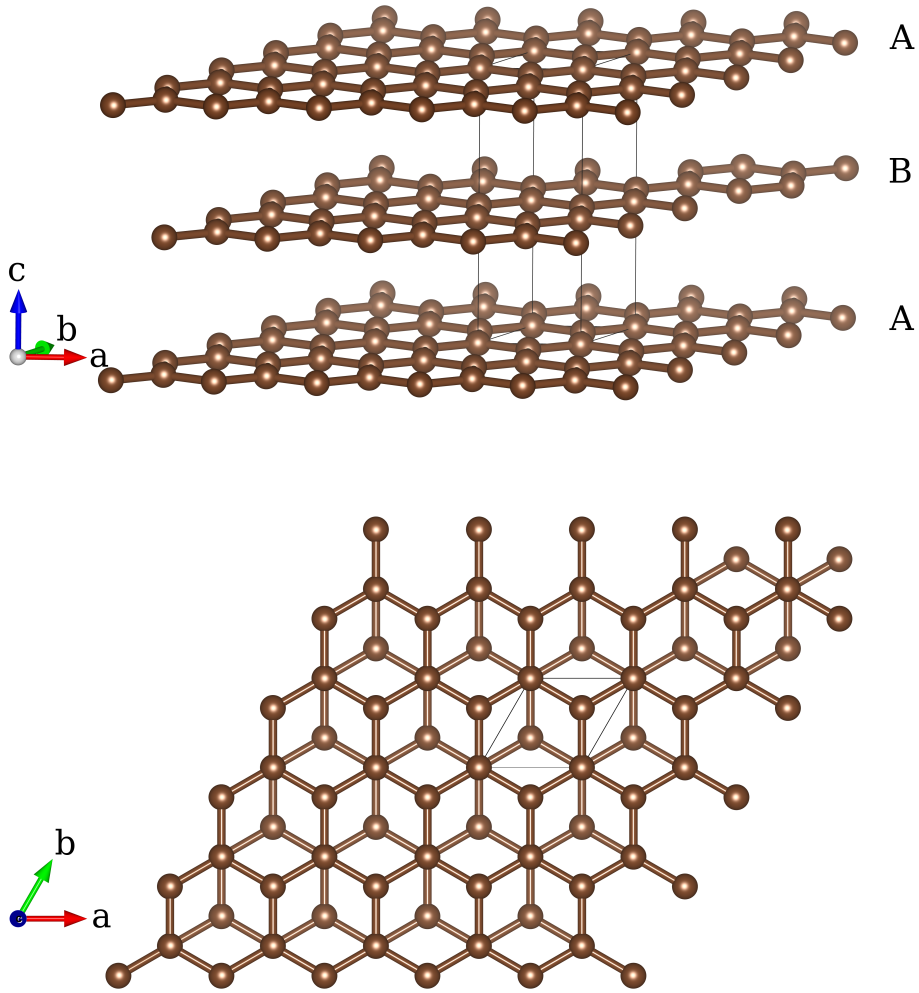


Figure 2.2: (a) A side-view of the atomic structure of graphite. Each of the layers is identical to a graphene layer shown in Figure 2.1, and the layers are labelled to show the AB stacking pattern. The distance between adjacent layers is 3.348 Å [32]. (b) A top-down view of graphite shows how the adjacent layers are positioned relative to each other. The central atom in each hexagon is from the B layer in (a).

## 2.2 Thermal transport by phonons

For the phonon contribution, the heat flux from Equation 2.1 can also be written as a sum over all possible phonon states: [24]

$$j^{\alpha} = \frac{1}{\Omega} \sum_{\lambda} f_{\lambda} E_{\lambda} v_{\lambda}^{\alpha}, \tag{2.9}$$

where $\lambda$ is a label for the state of the phonon, which will be defined later. $f_{\lambda}$ is the distribution function, which represents the occupation number: the number of phonons that are in that state. $E_{\lambda}$ is the phonon energy, and $v_{\lambda}^{\alpha}$ is the velocity of the phonon in the $\alpha$ direction. $\Omega$ here is the volume of the sample. The result is the rate at which energy flows through a surface perpendicular to $\alpha$.

The equation for the thermal conductivity is obtained by combining Equation 2.1 and Equation 2.9:

$$\kappa^{\alpha\beta} = -\frac{1}{\Omega \nabla^{\beta} T} \sum_{\lambda} f_{\lambda} E_{\lambda} v_{\lambda}^{\alpha}. \tag{2.10}$$

In order to calculate the thermal conductivity for a given system, the energy, $E_{\lambda}$, the velocity, $v_{\lambda}^{\alpha}$, and the distribution function, $f_{\lambda}$, of the heat carriers must be calculated first. In the following sections, the procedure for obtaining each of these quantities is described.

### 2.2.1 Phonons

As mentioned in the introduction to this chapter, phonons are usually the dominant contributor to the thermal transport in semiconductors and insulators. A phonon is a quasiparticle representing the normal modes of atomic vibrations in a lattice. Each phonon has a well-defined energy and velocity, which are determined by its state, $\lambda$. To calculate these values, the energetics of the system must be properly modelled first.

The theory of phonons is developed by first taking the Taylor expansion of the lattice potential energy $\Phi$ about its equilibrium value $\Phi_0$ for small atomic displacements

$\boldsymbol{u}_i$ away from the equilibrium positions $\boldsymbol{r}_i^0$:

$$\Phi(\boldsymbol{r}_1^0 + \boldsymbol{u}_1, \boldsymbol{r}_2^0 + \boldsymbol{u}_2, ...) = \Phi_0 + \sum_{i,\alpha} \Phi_i^\alpha u_i^\alpha + \sum_{ij,\alpha\beta} \Phi_{ij}^{\alpha\beta} u_i^\alpha u_j^\beta + \sum_{ijk,\alpha\beta\gamma} \Phi_{ijk}^{\alpha\beta\gamma} u_i^\alpha u_j^\beta u_k^\gamma + ..., \tag{2.11}$$

where

$$\Phi_i^\alpha = \left.\frac{\partial \Phi}{\partial r_i^\alpha}\right|_0 \tag{2.12}$$

$$\Phi_{ij}^{\alpha\beta} = \left.\frac{\partial^2 \Phi}{\partial r_i^\alpha \partial r_j^\beta}\right|_0 \tag{2.13}$$

$$\Phi_{ijk}^{\alpha\beta\gamma} = \left.\frac{\partial^3 \Phi}{\partial r_i^\alpha \partial r_j^\beta \partial r_k^\gamma}\right|_0 . \tag{2.14}$$

Here, the Latin subscripts, $ijk$, are atomic indices, and the Greek superscripts, $\alpha\beta\gamma$, once again represent the Cartesian directions. Equations 2.12, 2.13, and 2.14 are the first-, second-, and third-order interatomic force constants (IFCs) respectively. $\Phi_0$ is the equilibrium potential energy of the system, so the first-order IFCs must vanish since the atoms are at their equilibrium positions (i.e. $\boldsymbol{F}_i = -\boldsymbol{\nabla}_i \Phi_0 = \boldsymbol{0}$). The first non-zero term after the ground state energy is the second-order correction. Including only the second-order correction is equivalent to making the approximation that all of the atoms in a material behave as though they were a system of masses and springs. This is known as the harmonic approximation. As will be shown next, the phonon energies and velocities are obtained from the harmonic approximation. Higher-order terms in Equation 2.11 capture the phonon scattering properties, which will be shown later.

### 2.2.2 The Harmonic Approximation

The dynamics of each atom is described by solving the appropriate equation of motion

$$F_i^\alpha = -\frac{\partial \Phi}{\partial u_i^\alpha} = M_i \ddot{u}_i^\alpha \tag{2.15}$$

Here, $M_i$ is the mass of the $i$th atom, and $\ddot{u}_i^\alpha$ is the second time-derivative of the atomic displacement vector $\boldsymbol{u}_i$ in the $\alpha$ direction. Substituting Equation 2.11, keeping only up to second-order, into Equation 2.15 results in

$$M_i \ddot{u}_i^\alpha = -\sum_j \Phi_{ij}^{\alpha\beta} u_j^\beta. \tag{2.16}$$

Solutions to this system of equations take the form of plane waves [30]

$$u_i^\alpha(\boldsymbol{q}; \boldsymbol{R}) = \frac{1}{\sqrt{M_i}} \epsilon_i^\alpha(\boldsymbol{q}) e^{i(\boldsymbol{q}\cdot\boldsymbol{R} + \omega(\boldsymbol{q})t)}, \tag{2.17}$$

where $\boldsymbol{q}$ is the wavevector, and $\omega(\boldsymbol{q})$ is the angular frequency. $\epsilon_i^\alpha$ is the polarization vector, which determines the amplitude of oscillation of atom $i$ in the $\alpha$ direction, and $\boldsymbol{R}$ is a lattice vector, as defined in Section 2.1. Due to the periodic nature of a crystal, solutions are only required for the atoms in the first unit cell ($\boldsymbol{R} = 0$). The motion of an atom $i$ in a unit cell that is a displacement $\boldsymbol{R}$ away from the first unit cell is simply out of phase with the same atom $i$ in the first unit cell by $e^{i\boldsymbol{q}\cdot\boldsymbol{R}}$.

Substituting 2.17 into the equations of motion (Equation 2.15) results in

$$\sqrt{M_i}\omega^2(\boldsymbol{q})\epsilon_i^\alpha(\boldsymbol{q}) = \sum_{j,R'} \Phi_{ij}^{\alpha\beta}(\boldsymbol{R}, \boldsymbol{R}') \frac{1}{\sqrt{M_j}} \epsilon_j^\beta(\boldsymbol{q}) e^{i\boldsymbol{q}\cdot(\boldsymbol{R}' - \boldsymbol{R})}. \tag{2.18}$$

The choice for $\boldsymbol{R}$ is arbitrary since each unit cell is identical, so $\boldsymbol{R}$ can be taken to be $\boldsymbol{0}$. The sum can also be broken up into two sums, one over the atomic indices, $i$, of atoms within the first unit cell, and another over all unit cells, at $\boldsymbol{R}'$, in the crystals:

$$\omega^2(\boldsymbol{q})\epsilon_i^\alpha(\boldsymbol{q}) = \sum_j \epsilon_j^\beta(\boldsymbol{q}) \frac{1}{\sqrt{M_i M_j}} \sum_{\boldsymbol{R}'} \Phi_{ij}^{\alpha\beta}(\boldsymbol{R}') e^{i\boldsymbol{q}\cdot\boldsymbol{R}'}. \tag{2.19}$$

The sum over $\boldsymbol{R}'$ is the Fourier transform of the second-order IFCs $\widetilde{\Phi}_{ij}^{\alpha\beta}(\boldsymbol{q})$:

$$\widetilde{\Phi}_{ij}^{\alpha\beta}(\boldsymbol{q}) = \sum_{\boldsymbol{R}'} \Phi_{ij}^{\alpha\beta}(\boldsymbol{R}') e^{i\boldsymbol{q}\cdot\boldsymbol{R}'}. \tag{2.20}$$

The interaction is short-ranged, so in the sum over $\boldsymbol{R}'$ is usually truncated to a few of the closest unit cells. The mass-normalized Fourier transform is called the Dynamical

matrix:

$$D_{ij}^{\alpha\beta}(\boldsymbol{q}) = \frac{1}{\sqrt{M_i M_j}} \widetilde{\Phi}_{ij}^{\alpha\beta}. \tag{2.21}$$

Substituting this into Equation 2.19 results in

$$\omega^2(\boldsymbol{q})\epsilon_i^{\alpha}(\boldsymbol{q}) = \sum_j D_{ij}^{\alpha\beta}(\boldsymbol{q})\epsilon_j^{\beta}(\boldsymbol{q}). \tag{2.22}$$

In vector form, this equation is equivalent to

$$\boldsymbol{D}(\boldsymbol{q})\boldsymbol{\epsilon}(p,\boldsymbol{q}) = \omega^2(p,\boldsymbol{q})\boldsymbol{\epsilon}(p,\boldsymbol{q}), \tag{2.23}$$

which is simply an eigenvalue problem for the dynamical matrix $D_{ij}^{\alpha\beta}(\boldsymbol{q})$, with eigenvectors $\boldsymbol{\epsilon}(p,\boldsymbol{q})$, and eigenvalues $\omega^2(p,\boldsymbol{q})$. Here, $p$ was introduced as a label for the $3N$ solutions to Equation 2.23, where $N$ is the number of atoms in the primitive cell. The state of a phonon, and therefore its energy and velocity, is completely described by $p$ and $\boldsymbol{q}$. In the introduction to this section, $\lambda$ was used as a label for phonon modes. In the following discussion $\lambda$ will still sometimes be used when it is convenient, but note that $\lambda = (p,\boldsymbol{q})$.

The energy of a phonon is

$$E(p,\boldsymbol{q}) = \hbar\omega(p,\boldsymbol{q}), \tag{2.24}$$

where $\hbar$ is the reduced Planck's constant. Therefore, the full phonon dispersion can be calculated by constructing $\boldsymbol{D}(\boldsymbol{q})$ and then solving Equation 2.23 for all wavevectors $\boldsymbol{q}$.

There are an infinite number of wavevectors; however, they exist in reciprocal space, which is periodic. The Brillouin zone (BZ) is the first Wigner-Seitz unit cell in reciprocal space, and contains all non-equivalent $\boldsymbol{q}$ vectors. The wavevectors in all other unit cells in reciprocal space are equivalent to a vector within the BZ, so only $\boldsymbol{q}$ in the first BZ are required for a full solution. The group velocity of each phonon mode can then be calculated in the usual way

$$\boldsymbol{v}(p,\boldsymbol{q}) = \boldsymbol{\nabla}_{\boldsymbol{q}}\omega(p,\boldsymbol{q}). \tag{2.25}$$

The phonon energies (Equation 2.24) and velocities (Equation 2.25) are two of the three variables required in order to calculate the thermal conductivity in Equation 2.10. The final component is the distribution function $f_\lambda$, which is obtained by solving the Boltzmann Transport Equation (BTE).

## 2.3 The Boltzmann Transport Equation

The distribution function, $f(\boldsymbol{r}, \boldsymbol{p}, t)$, describes the occupation of each state, which depends on their position ($\boldsymbol{r}$) and momentum ($\boldsymbol{p}$) at a given time ($t$). The Boltzmann transport equation (BTE) describes the evolution of $f(\boldsymbol{r}, \boldsymbol{p}, t)$ [33, 34].

$$\frac{\partial f}{\partial t} + \boldsymbol{v} \cdot \boldsymbol{\nabla}_{\boldsymbol{r}} f + \boldsymbol{F} \cdot \boldsymbol{\nabla}_{\boldsymbol{p}} f = \left.\frac{\partial f}{\partial t}\right|_{\text{scatter}}. \tag{2.26}$$

From left to right in the equation, it describes how any changes in the population of a state can arise due to diffusion, external forces, or scattering.

There are no external forces acting on phonons ($\boldsymbol{F} = \boldsymbol{0}$), or sources/sinks, so the form of the equation that must be solved in the steady state is

$$\boldsymbol{v} \cdot \boldsymbol{\nabla}_{\boldsymbol{r}} T \frac{\partial f}{\partial T} = \left.\frac{\partial f}{\partial t}\right|_{\text{scatter}}, \tag{2.27}$$

This is sometimes called the Peierls-Boltzmann Equation (PBE) [33, 35].

In thermal equilibrium, the phonon distribution function is given by the Bose-Einstein distribution $f^0$:

$$f^0(\omega(p, \boldsymbol{q}), T) = \frac{1}{e^{\hbar\omega(p,\boldsymbol{q})/k_B T} - 1}, \tag{2.28}$$

where $k_B$ is Boltzmann's constant, and $T$ is the temperature of the system. However, there is no net heat flow in thermal equilibrium. Applying a temperature gradient $\boldsymbol{\nabla}_{\boldsymbol{r}} T \neq 0$ causes the distribution function to deviate from $f^0$, resulting in a net heat current. This new distribution is found by solving the BTE. In the following discussion, $\lambda$ subscripts will be used to imply a dependence on $p$ and $\boldsymbol{q}$.

A common approach to solving the BTE is to expand $f_0$ to first-order [33]:

$$f_\lambda = f^0_\lambda - \boldsymbol{l}_\lambda \cdot \boldsymbol{\nabla}_{\boldsymbol{r}} T \frac{\partial f^0_\lambda}{\partial T}. \tag{2.29}$$

Combining Equations 2.27 and 2.29 results in the linearized BTE [24]

$$\boldsymbol{l}_\lambda = \tau_\lambda^0(\boldsymbol{v}_\lambda + \boldsymbol{\Delta}_\lambda), \tag{2.30}$$

where $\tau_\lambda^0$ is the relaxation time. In the relaxation time approximation (RTA), it is assumed that the system relaxes back to the equilibrium distribution function $f_\lambda^0$ in a characteristic time $\tau^0$. Taking $\boldsymbol{l}_\lambda = \tau_\lambda^0 \boldsymbol{v}_\lambda$ is equivalent to the RTA, so the linear expansion of $f_\lambda$ goes beyond the RTA with the addition of a correction term $\boldsymbol{\Delta}_\lambda$. The equation for $\boldsymbol{\Delta}_\lambda$ is:

$$\begin{aligned}\boldsymbol{\Delta}_\lambda =& \frac{1}{N_q}\sum_{\lambda'\lambda''}^{+}\Gamma^{+}_{\lambda\lambda'\lambda''}(\xi_{\lambda,\lambda''}\boldsymbol{l}_{\lambda''} - \xi_{\lambda\lambda'}\boldsymbol{l}_{\lambda'}) \\ &+ \frac{1}{N_q}\sum_{\lambda'\lambda''}^{-}\Gamma^{-}_{\lambda\lambda'\lambda''}(\xi_{\lambda,\lambda''}\boldsymbol{l}_{\lambda''} + \xi_{\lambda\lambda'}\boldsymbol{l}_{\lambda'}),\end{aligned} \tag{2.31}$$

where $N_q$ is the number of wavevectors in the discretized BZ. $\xi_{\lambda\lambda'} = \omega_{\lambda'}/\omega_\lambda$, and $\Gamma^{\pm}_{\lambda\lambda'\lambda''}$ are the three-phonon scattering rates. The scattering rates are obtained using Fermi's golden rule, and are described in the following section. The equation for thermal conductivity, using the linearized BTE, becomes [24]

$$\kappa^{\alpha\beta} = \frac{1}{k_B T^2 \Omega N_q}\sum_\lambda f_\lambda^0(f_\lambda^0+1)(\hbar\omega_\lambda)^2 v_\lambda^\alpha F_\lambda^\beta. \tag{2.32}$$

Equation 2.30 can be solved iteratively [36], beginning with the RTA, and using Equation 2.31. In practice, the iterative process repeats until the thermal conductivity, calculated using Equation 2.32, converges. The final requirement to solve the BTE and calculate the thermal properties is to supply it with the three-phonon scattering rates.

## 2.4 Phonon Scattering

Phonons are able to scatter with other phonons, boundaries, electrons, impurities, etc. All of these scattering events can contribute to thermal resistance by altering the phonon momentum. For most semiconductors at room temperature, the dominant mechanism is phonon-phonon scattering, so the others are left out of the following

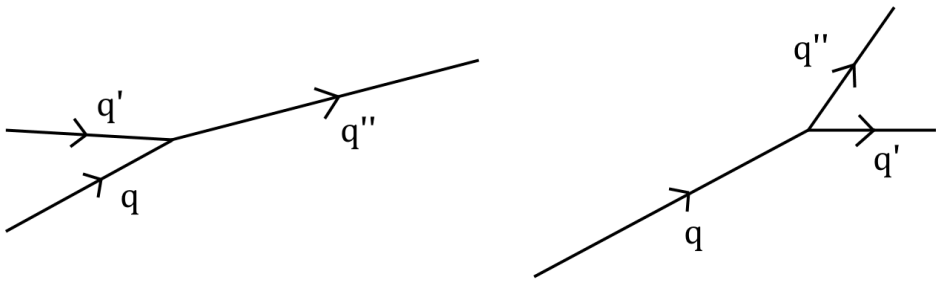


(a) (b)

Figure 2.3: (a) Phonon absorption process, where phonons with wavevectors $\boldsymbol{q}$ and $\boldsymbol{q}'$ combine to a single phonon with wavevector $\boldsymbol{q}''$. (b) Phonon emission process, where a single phonon with wavevector $\boldsymbol{q}$ splits into two phonons with wavectors $\boldsymbol{q}'$ and $\boldsymbol{q}''$.

discussion [33, 37].

Specifically, three-phonon scattering is the primary contributer to the thermal conductivity in most cases. There are two processes through which three phonons can interact: absorption, and emission (see figure 2.3). Absorption occurs when two incident phonons, with wavevectors $\boldsymbol{q}$ and $\boldsymbol{q}'$, scatter into a third state, $\boldsymbol{q}''$. An emission process is when a single phonon, $\boldsymbol{q}$, scatters into two phonons, $\boldsymbol{q}'$ and $\boldsymbol{q}''$.

During these processes, energy and crystal momentum must be conserved. The crystal momentum of phonons is $\hbar\boldsymbol{q}$, and must be conserved to within a reciprocal lattice vector $\boldsymbol{Q}$:

$$\boldsymbol{q} \pm \boldsymbol{q}' = \boldsymbol{q}'' + \boldsymbol{Q}. \tag{2.33}$$

The corresponding energy conservation equation is

$$\hbar\omega \pm \hbar\omega' = \hbar\omega'' \tag{2.34}$$

The positive signs are chosen for phonon absorption, and the negative signs are for phonon emission. The addition of $\boldsymbol{Q}$ appears in Equation 2.33 because any phonon with a wavevector $\boldsymbol{q}$ that is outside of the first BZ is indistinguishable from a phonon with a wavevector $\boldsymbol{q} + \boldsymbol{Q}$ within the first BZ.

These scattering processes are further subdivided into either normal or Umklapp processes depending on whether or not $\boldsymbol{Q}$ is non-zero. When $\boldsymbol{q} \pm \boldsymbol{q}'$ is within the first

BZ, then $\boldsymbol{Q} = \boldsymbol{0}$, which is a normal process. When it falls outside of the first BZ, then $\boldsymbol{Q} \neq \boldsymbol{0}$, and it is an Umklapp process. Both processes contribute to the thermal conductivity by altering the population of phonons in a given state, and by scattering to states that modify the direction of the velocity of the phonons.

The three-phonon scattering rates are obtained using Fermi's Golden Rule, and are expressed as [24]

$$\Gamma^{+}_{\lambda\lambda'\lambda''} = \frac{\hbar\pi}{4}\frac{f_0' - f_0''}{\omega_\lambda\omega_{\lambda'}\omega_{\lambda''}}|V^{+}_{\lambda\lambda'\lambda''}|^2\delta(\omega_\lambda + \omega_{\lambda'} - \omega_{\lambda''}), \tag{2.35}$$

$$\Gamma^{-}_{\lambda\lambda'\lambda''} = \frac{\hbar\pi}{4}\frac{f_0' + f_0'' + 1}{\omega_\lambda\omega_{\lambda'}\omega_{\lambda''}}|V^{-}_{\lambda\lambda'\lambda''}|^2\delta(\omega_\lambda - \omega_{\lambda'} - \omega_{\lambda''}). \tag{2.36}$$

Here, $f^0$ is the Bose-Einstein distribution, $V^{\pm}_{\lambda\lambda'\lambda''}$ are the scattering matrix elements, and the Dirac deltas impose conservation of energy. The scattering matrix elements are given as

$$V^{\pm}_{\lambda\lambda'\lambda''} = \sum_{i\in\text{u.c.}}\sum_{j,k}\sum_{\alpha\beta\gamma}\Phi^{\alpha\beta\gamma}_{ijk}\frac{\epsilon^{\alpha}_i(\lambda)\epsilon^{\beta}_j(p', \pm\boldsymbol{q'})\epsilon^{\gamma}_k(p'', -\boldsymbol{q''})}{\sqrt{M_iM_jM_k}}, \tag{2.37}$$

where the $\epsilon$'s are the eigenvectors described in Subsection 2.2.2, $\Phi^{\alpha\beta\gamma}_{ijk}$ are the third-order IFCs described in Section 2.2.1, and $M_i$,$M_j$ and $M_k$ are the masses of atoms $i$, $j$, and $k$ respectively.

At this point in the discussion, all of the variables required to calculated the lattice thermal conductivity depend only on the second- and third-order IFCs. The phonon dispersion can be calculated using the second-order IFCs, which provides the phonon energies and velocities. Solutions to the BTE depend on these variables, along with the three-phonon scattering rates, which require the third-order IFCs. It is possible to calculate accurate values of the IFCs from first-principles, using Density Functional Theory (DFT).

## 2.5 Density-Functional Theory

DFT is an ab initio method that can be used to calculate IFCs. At its heart, this method converts the full quantum many-body problem into an effective single-particle Schrödinger equation. The basic principle of DFT is that the electronic ground-state

energy $E_{GS}$ of a many-body system is a unique functional of the electron density $n(\boldsymbol{r})$ [38]. This functional is also variational, so the ground-state energy can be found by minimizing the energy with respect to $n(\boldsymbol{r})$.

In 1965, Kohn and Sham showed that solutions for $n(\boldsymbol{r})$ can be obtained by solving a single-particle Schrödinger equation with an effective potential [39]:

$$[\hat{T} + V_{\mathrm{KS}}(\boldsymbol{r})]\psi_i(\boldsymbol{r}) = E_i\psi_i(\boldsymbol{r}). \tag{2.38}$$

Here, $\hat{T}$ is the standard kinetic energy operator, $V_{KS}$ is the effective, or Kohn-Sham, potential, $\psi_i(\boldsymbol{r})$ are the Kohn-Sham orbitals, and $E_i$ is the energy of the $i$th orbital. The forms of $\hat{T}$ and $V_{\mathrm{KS}}$ are not shown here, but interested readers can find the details in [39]. The electron density is then obtained in the usual way:

$$n(\boldsymbol{r}) = 2\sum_{i=1}^{N/2} |\psi_i(\boldsymbol{r})|^2, \tag{2.39}$$

where $N$ is the number of electrons, and the 2 in front of the sum accounts for spin degeneracy.

The Kohn-Sham potential is itself a functional of the electron density $V_{\mathrm{KS}}[n(\boldsymbol{r})]$. This allows the Kohn-Sham equations to be solved self-consistently. The density $n(\boldsymbol{r})$ is used to construct the effective potential $V_{\mathrm{KS}}$, which is then used to solve for the Kohn-Sham orbitals in Equation 2.38. The orbitals are then used to calculate the density (Equation 2.39), which should be same as the input density when self-consistency is achieved.

One problem is that the effective potential requires an exchange-correlation potential. There is no known functional that captures this interaction perfectly, so approximations are required. Many approximations to this functional have been proposed, the simplest is the Local Density Approximation (LDA) [39]. The basis of the LDA is that a small volume of electrons of density $n(\boldsymbol{r})$ will contribute an exchange-correlation energy equal to that of a uniform electron gas of the same density and volume. This is an adequate approximation in systems with slowly-varying, or high, electron densities, but produces poor results in most real systems where fluctuations in the density can be large. A significant improvement is the Generalized Gradient

Approximation (GGA) [40], which uses the gradient of the electron density, $\boldsymbol{\nabla}_{\boldsymbol{r}} n(\boldsymbol{r})$, as a correction. The GGA was chosen for the calculations in this thesis.

There are two main methods of calculating the second-order IFCs: finite difference (FD) and density-functional perturbation theory (DFPT). The former is more physically intuitive. The ground state energy is first calculated for the system in equilibrium, $E_0 = (\boldsymbol{r}_1^0, \boldsymbol{r}_2^0, ...)$, where $\boldsymbol{r}_i^0$ are the equilibrium positions of the atoms. The energy is then recalculated for small atomic displacements $\Delta r_i^\alpha$, where $\alpha$ is the Cartesian direction, $E_i^\alpha = E(\boldsymbol{r}_1^0, ..., \boldsymbol{r}_i^0 + \Delta r_i^\alpha, ...)$ and $E_j^\beta = E(\boldsymbol{r}_1^0, ..., \boldsymbol{r}_j^0 + \Delta r_j^\beta, ...)$. The force constants are then approximated as

$$\Phi_{ij}^{\alpha\beta} = \frac{\partial^2 \Phi_0}{\partial r_i^\alpha \partial r_j^\beta} \approx \frac{E_i^\alpha + E_j^\beta - 2E_0}{\Delta r_i^\alpha \Delta r_j^\beta}. \tag{2.40}$$

Each of these energies are calculated using DFT. The number of DFT calculations that would be required to perform these calculations would be immense, since at least nine energy values are required for each pair of atoms. For phonon calculations, IFCs are usually required between atoms that are several unit cells away. This requires the construction of a supercell, which can contain hundreds of atoms, even for simple systems like graphene and graphite. In practice, the symmetries of the crystal structure are exploited to reduce the total number of calculations that are required.

In this work, the second-order IFCs are calculated using DFPT. For DFPT, the dynamical matrix from Section 2.2.1 is calculated directly for each $\boldsymbol{q}$ [41]. This is done by treating the displacements of atoms for each phonon mode as a small perturbation from the ground state. Perturbation theory is then used to solve for the Fourier transform of the second-order IFCs, which are used to get the dynamical matrix directly.

The third-order IFCs are then calculated using the FD method for third-order derivatives:

$$\Phi_{ijk}^{\alpha\beta\gamma} = \frac{\partial^3 \Phi_0}{\partial r_i^\alpha \partial r_j^\beta \partial r_k^\gamma} \approx \frac{E_i^\alpha + E_j^\beta + E_k^\gamma - 3E_0}{\Delta r_i^\alpha \Delta r_j^\beta \Delta r_k^\gamma}. \tag{2.41}$$

This is the final component required to calculate the three-phonon scattering rates, and by extension the thermal conductivity.

## 2.6 Phonon Selection Rules

The materials studied in this thesis have particular symmetries that affect what scattering processes are possible, and thus affect their thermal transport properties. Specifically, some three-phonon scattering mechanisms are forbidden due to the symmetries of the system. In the case of graphene, mirror symmetry about the plane of carbon atoms produces selection rules, which drastically reduces the number of scattering processes available to certain phonon modes [25]. This is one of the factors that is thought to lead to the large thermal conductivity of graphene of up to 5000 $\mathrm{W\,m^{-1}\,K^{-1}}$.

The carbon atoms in graphene are located entirely within a single plane, which is usually taken to be the $xy$ plane. Each correction to the lattice potential given in Equation 2.11 must be invariant under any symmetry operation [26]. For the second-order correction, this invariance is stated as:

$$\sum_{ij}\sum_{\alpha\beta}\Phi_{ij}^{\alpha\beta}u_i^{\alpha}u_j^{\beta}=\sum_{i'j'}\sum_{\alpha'\beta'}\Phi_{i'j'}^{\alpha'\beta'}u_{i'}^{\alpha'}u_{j'}^{\beta'}, \tag{2.42}$$

where the primed indices represent the new indices after a symmetry operation. Since all of the carbon atoms are within the $xy$ plane, they are all mapped to themselves for a reflection about the $z$ axis, so the atomic indices, $i$ and $j$, remain unchanged. The same is true for the component labels, $\alpha$ and $\beta$. The only difference is if $\alpha$ or $\beta$ are $z$, then the direction of the corresponding displacement vector component is reversed, so $u_i^{\alpha}$ becomes $-u_i^{\alpha}$. Therefore, Equation 2.42 becomes

$$\sum_{ij}\sum_{\alpha\beta}\Phi_{ij}^{\alpha\beta}u_i^{\alpha}u_j^{\beta}=\sum_{ij}\sum_{\alpha\beta}(-1)^m\Phi_{ij}^{\alpha\beta}u_i^{\alpha}u_j^{\beta}, \tag{2.43}$$

which requires that

$$\Phi_{ij}^{\alpha\beta}=(-1)^m\Phi_{ij}^{\alpha\beta}. \tag{2.44}$$

Here, $m$ is the number of occurences of $z$ in $\alpha\beta$. In order for this to hold, $\Phi_{ij}^{\alpha\beta}$ must vanish for terms with a single $z$ component in $\alpha\beta$.

It is straightforward to extend this analysis to the higher-order IFCs. For the

third-order IFCs, the symmetry requirement is

$$\Phi_{ijk}^{\alpha\beta\gamma} = (-1)^m \Phi_{ijk}^{\alpha\beta\gamma}, \tag{2.45}$$

so any terms where $\alpha\beta\gamma$ contains an odd number of $z$'s must be zero. In general, any order IFC with an odd number of $z$ components must be zero because of the mirror symmetry about the $z$ axis.

A consequence of Equation 2.44 is that the atoms in graphene are restricted to only move either in the $z$ direction or within the $xy$ plane. When constructing the dynamical matrix from its definition in Equations 2.21 and 2.20, the off-diagonal terms with z components must be zero:

$$D_{ij}^{\alpha\beta} = \begin{pmatrix} D_{ij}^{xx} & D_{ij}^{xy} & 0 \\ D_{ij}^{yx} & D_{ij}^{yy} & 0 \\ 0 & 0 & D_{ij}^{zz} \end{pmatrix}. \tag{2.46}$$

Therefore, there is a complete decoupling between the $xy$ and $z$ directions, so the eigenvectors will be decoupled in the same way:

$$\boldsymbol{\epsilon}_i(\boldsymbol{q}) = \begin{pmatrix} \epsilon_i^x(\boldsymbol{q}) \\ \epsilon_i^y(\boldsymbol{q}) \\ 0 \end{pmatrix} \text{ or } \begin{pmatrix} 0 \\ 0 \\ \epsilon_i^z(\boldsymbol{q}) \end{pmatrix}. \tag{2.47}$$

The eigenvectors with only a $z$ component correspond to flexural phonon modes, while eigenvectors without a $z$ component correspond to the longitudinal and transverse modes.

These symmetries result in a large reduction in the number of scattering processes that are available to the flexural phonon modes in graphene. The flexural acoustic (ZA) modes in graphene are modes where both carbon atoms in the unit cell move in the $z$ direction. The other two acoustic modes correspond to transverse, TA, and longitudinal, LA, modes where motion is restricted to the $xy$ plane.

This has important implications for the scattering rates since the scattering matrix elements depend on the eigenvectors (see Equation 2.37). The number of terms in the sums are drastically reduced for scattering processes that involve flexural phonons.

For example, if only one of the incident phonons is flexural, then the scattering matrix element can be written as

$$V^{\pm}(\text{flex}, \lambda', \lambda'') = \sum_{i \in \text{u.c.}} \sum_{j,k} \sum_{\beta\gamma}^{xy} \Phi_{ijk}^{z\beta\gamma} \frac{\epsilon_i^z(\text{flex}) \epsilon_j^{\beta}(p', \pm \boldsymbol{q}') \epsilon_k^{\gamma}(p'', -\boldsymbol{q}'')}{\sqrt{M_i M_j M_k}}. \tag{2.48}$$

The $\alpha$ became $z$ since the flexural phonon eigenvectors only have non-zero $z$ components. Assuming the other two phonons are not flexural, only the $x$ and $y$ components of $\epsilon_j^{\beta}$ and $\epsilon_k^{\gamma}$ are non-zero. The remaining terms contain third-order IFCs with a single $z$ component, which must be zero because of Equation 2.45.

Similarly, the scattering matrix elements for processes involving 3 flexural phonons are written as

$$V^{\pm}(\text{flex}, \text{flex}', \text{flex}'') = \sum_{i \in \text{u.c.}} \sum_{j,k} \Phi_{ijk}^{zzz} \frac{\epsilon_i^z(\text{flex}) \epsilon_j^z(\text{flex}') \epsilon_k^z(\text{flex}'')}{\sqrt{M_i M_j M_k}}, \tag{2.49}$$

where this time the third-order IFCs all have three $z$ components, which are once again zero because of Equation 2.45. This means that all three-phonon processes where all three phonons are flexural are forbidden as well. This argument does not work for processes with an even number of flexural phonons since third-order IFCs with an even number of $z$ components are not necessarily zero. Therefore, the phonon selection rules are that any three-phonon scattering process containing an odd number of flexural phonons are forbidden due to reflection symmetry about the $z$ axis.

The selection rules for graphene reduce the scattering probability and are one reason why the thermal conductivity is so high. The ZA phonons contribute more to the thermal conductivity than the other modes due to the limited number of scattering pathways.

As soon as the mirror symmetry is broken, the selection rules no longer hold, and the thermal conductivity will decrease. This is observed when graphene is supported by a substrate, and in few-layer graphene [26, 27]. It is important to note that this mirror symmetry still exists in graphite, but the atoms are not all mapped onto themselves by the symmetry operation. This results in a reduced set of selection rules. The focus of this study is on graphene and graphite, so understanding how the selection rules, and lack thereof, influence the thermal transport properties is vital

for understanding the transition from 3D to 2D transport.

# Chapter 3

# Results

The purpose of this study was to understand how thermal transport properties vary when going from 3D to 2D materials. This is illustrated using graphite, where the two limiting cases are bulk graphite and monolayer graphene. The transition is studied by stretching the layers of graphite apart until they are effectively graphene monolayers.

The following sections begin with a short description of the numerical details. Next, the major results for graphene are presented first, because of their relatively simple form, and since they have been previously reported by others. The results for graphite will follow with a more in-depth analysis and will be compared to the results for graphene. The two limiting cases provide some insight on how the thermal properties should behave during the transition from 3D to 2D. Finally, a section comparing the stretched cases will complete the chapter.

## 3.1 Numerical Details

The electronic structure of each case was calculated using the PWscf package from the suite of DFT codes provided by Quantum Espresso (QE) [22]. The second-order IFCs, phonon eigenvectors, and phonon dispersions were obtained using the PHonon package from QE. The iterative solutions to the BTE were calculated using the software ShengBTE. The third-order IFCs required as input for ShengBTE were calculated with the finite-displacement method within QE, using an auxiliary Python script provided by ShengBTE.

Both QE and ShengBTE require a set of converged input parameters for each system in order to produce reliable results. The input parameters are determined by systematically varying each of them individually until the energy of the system converges. The converged values for graphene and graphite are listed at the beginning of each their associated sections, and those for the stretched cases are identical to the parameters used for graphite.

The DFT calculations in QE use a plane-wave basis set. From Bloch's theorem, the electronic wavevefunctions $\psi_{n,\boldsymbol{k}}(\boldsymbol{r})$ in a periodic crystal can be written as

$$\psi_{n,\boldsymbol{k}}(\boldsymbol{r}) = u_{n,\boldsymbol{k}}(\boldsymbol{r})e^{i\boldsymbol{k}\cdot\boldsymbol{r}}, \tag{3.1}$$

where $\boldsymbol{k}$ is wavevector and $n$ is the branch index. These electron state variables are analogous to the wavevector $\boldsymbol{q}$ and branch index $p$ used for phonons. $u_{n,\boldsymbol{k}}(\boldsymbol{r})$ is a function with the periodicity of the lattice.

$u_{n,\boldsymbol{k}}(\boldsymbol{r})$ can be constructed by using a basis of plane waves with the periodicity of the crystal:

$$u_{n,\boldsymbol{k}}(r) = \frac{1}{\Omega}\sum_{\boldsymbol{K}} C_{n,\boldsymbol{k},\boldsymbol{K}} e^{i\boldsymbol{K}\cdot\boldsymbol{r}}, \tag{3.2}$$

where $\Omega$ is the volume of the unit cell, $C_{n,\boldsymbol{k},\boldsymbol{K}}$ are coefficients in the sum and $\boldsymbol{K}$ are the reciprocal lattice vectors, which ensures that $u_{n,\boldsymbol{k}}(r)$ has the periodicity of the lattice. The wavefunctions in Equation 3.1 become

$$\psi_{n,\boldsymbol{k}}(\boldsymbol{r}) = \frac{1}{\Omega}\sum_{\boldsymbol{K}} C_{n,\boldsymbol{k},\boldsymbol{K}} e^{i(\boldsymbol{k}+\boldsymbol{K})\cdot\boldsymbol{r}}. \tag{3.3}$$

The ground state of the system is determined by minimizing the energy of the system with respect to the coefficients.

Physical quantities, like the electron density, can be calculated as a summation in reciprocal space over the first Brillouin zone (BZ). A $k$-grid is usually specified, which determines how the BZ is discretized. A $N_1 \times N_2 \times N_3$ $k$-grid has $N_k = N_1 \times N_2 \times N_3$ uniformly-spaced wavevectors, $\boldsymbol{k}$, within the first BZ. The density of this grid is one of the parameters that must be converged.

A similar type of grid, called the $q$-grid, is specified for the phonon dispersion and scattering calculations. The $q$-grid is exactly the same as a $k$-grid, only the points correspond to phonon wavevectors, $\boldsymbol{q}$, as opposed to the electron wavevectors $\boldsymbol{k}$.

The completeness of the basis set is determined by the number of reciprocal lattice vectors $\boldsymbol{K}$ that are used in the sum in Equation 3.3. Large wavevectors correspond to large fluctuations in the wavefunction and electron densities, which correspond to large kinetic energies, and thus large $\boldsymbol{K}$ values. It is customary to specify cutoff energies for the wavefunctions and electron densities, where $\boldsymbol{K}$ vectors with energies above the cutoffs are excluded. This reduces the size of the basis set, thus reducing

the computational cost.

Pseudopotentials are also used to model the potential due to the core states in each atom as smoother functions, further reducing the size of the basis set required for the calculation. The pseudopotentials that were used for the carbon atoms in each of the following cases were Projector Augmented Wave (PAW) [42] with the Perdew-Burke-Erzenhoff (PBE) [43] GGA exchange-correlation functional.

For graphite, the layers are held together by the Van der Waals interaction. It is especially important to model these interactions correctly for this study since the changes in the thermal properties must be due to changes in interaction between layers. For this study, the Van der Waals interaction is modelled using the exchange-hole dipole moment (XDM) model [44, 45].

The converged parameters in each case were selected so that the total energy of the system was converged to within 0.1meV. For graphene, a 21x21x1 $k$-grid was used, with a wavefunction cutoff energy of 70 Ry, and a 2600 Ry density cutoff energy. The DFPT calculations were performed on a 9x9x1 $q$-grid. The ShengBTE calculations for thermal conductivity and phonon scattering propreties used a 60x60x1 $q$-grid.

For graphite, the calculations were performed using a 15x15x3 $k$-grid with a wavefunction cutoff energy of 60 Ry and a density cutoff of 400 Ry. The DFPT calculations were performed on a 6x6x3 $q$-grid, and the ShengBTE calculations used a 30x30x12 $q$-grid. The stretched cases of graphite all used the same parameters as graphite. All of the ShengBTE calculations were performed at 300 K.

## 3.2 Graphene

The results for graphene are presented first. This section will be a quick overview of the general properties of graphene, to serve as a reference, and to be compared to the other cases later.

The atomic structure was first relaxed by minimizing the total energy and forces with respect to the atomic positions. The energy threshold was $1 \times 10^{-6}$ Ry, and the

forces were converged to within $1 \times 10^{-5}$ Ry/$a_0$. The primitive lattice vectors are

$$\boldsymbol{a}_1 = a\hat{\boldsymbol{x}} \tag{3.4}$$

$$\boldsymbol{a}_2 = \frac{a}{2}\hat{\boldsymbol{x}} + \frac{\sqrt{3}a}{2}\hat{\boldsymbol{y}} \tag{3.5}$$

$$\boldsymbol{a}_3 = 10a\hat{\boldsymbol{z}}, \tag{3.6}$$

with a lattice constant $a = 2.4643$Å. The third lattice constant, $a_3$, was chosen so that the separation between the graphene layers are large enough that there is no measurable interaction between them. The two carbon atoms are located within the unit cell at $(0, 0, 0)$ and $(2/3, 2/3, 0)$ in crystal coordinates (i.e. in terms of the lattice vectors).

The phonon dispersion and density of states (DOS) of graphene are shown in Figure 3.1. The dispersion is consistent with previous calculations and experiments by other groups [46–48]. There are 6 different phonon branches in graphene, because there are two atoms in the unit cell. The bottom three are the acoustic phonon branches: longitudinal acoustic (LA), transverse acoustic (TA), and flexural acoustic (ZA). The ZA branch appears parabolic, due to the 2D nature which results in weak out-of-plane interactions, while the other acoustic branches are linear, as expected. In most bulk materials, all three acoustic branches are linear near $q = 0$.

The phonon density of states for a material depends on the shape of the phonon dispersion, and the dimensionality of the material. For a two-dimensional material like graphene, parabolic bands contribute a constant density of states, while the DOS from linear bands is linear with energy. Since the linear part is negligible at low energies, the DOS of graphene should be constant near 0 meV. The DOS in Figure 3.1 is nearly constant for most of the low-energy range, but goes to zero at $E = 0$ meV. This discrepancy is due to a slightly misshapen flexural phonon branch near 0 meV, and is discussed later in this chapter.

The three-phonon scattering rates were calculated at room temperature ($T = 300$ K), and plotted in Figure 3.2. The phonons in each of the acoustic branches are coloured and labeled over the first 50 meV so that they are distinguishable. Each point in Figure 3.2 corresponds to the scattering rate of a phonon with a particular $\boldsymbol{q}$ and $p$.

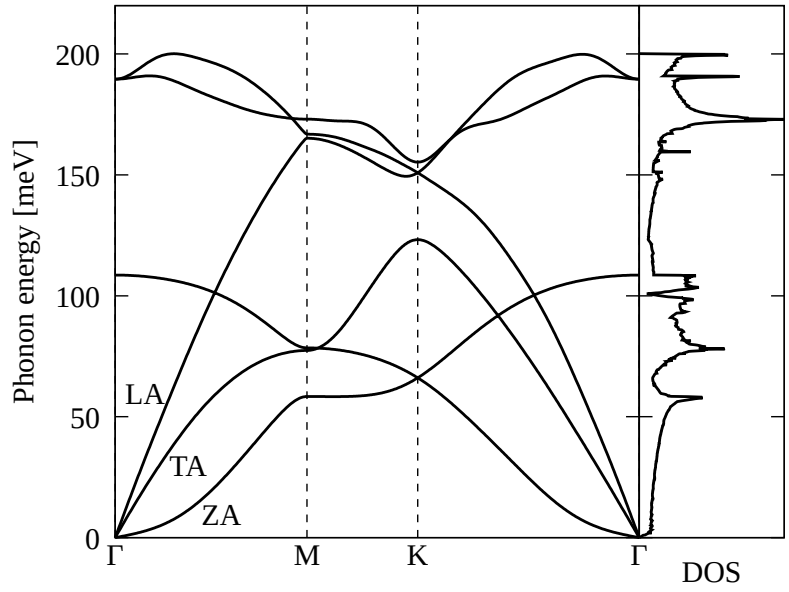


(a)

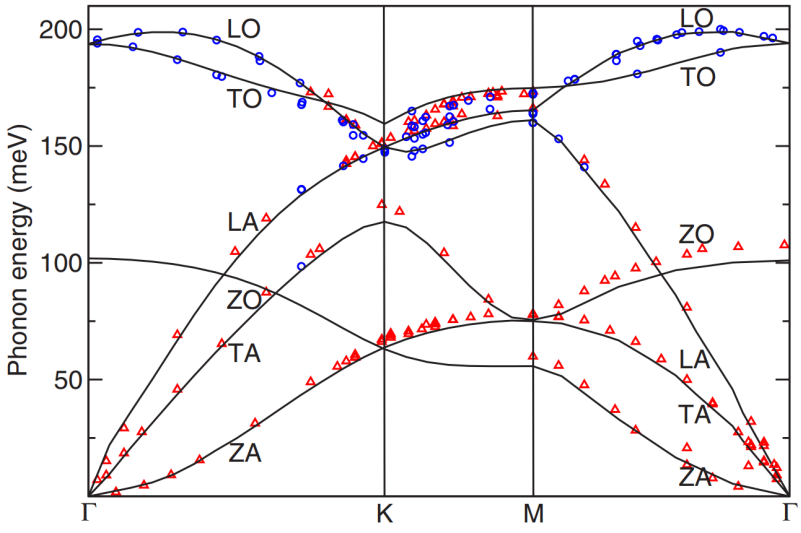


(b)

Figure 3.1: (a) Phonon dispersion and density of states of graphene calculated with QE. (b) Phonon dispersion from Ref [47] calculated using DFT (solid line), and experimental data from inelastic x-ray scattering (red triangles and blue circles [46]).

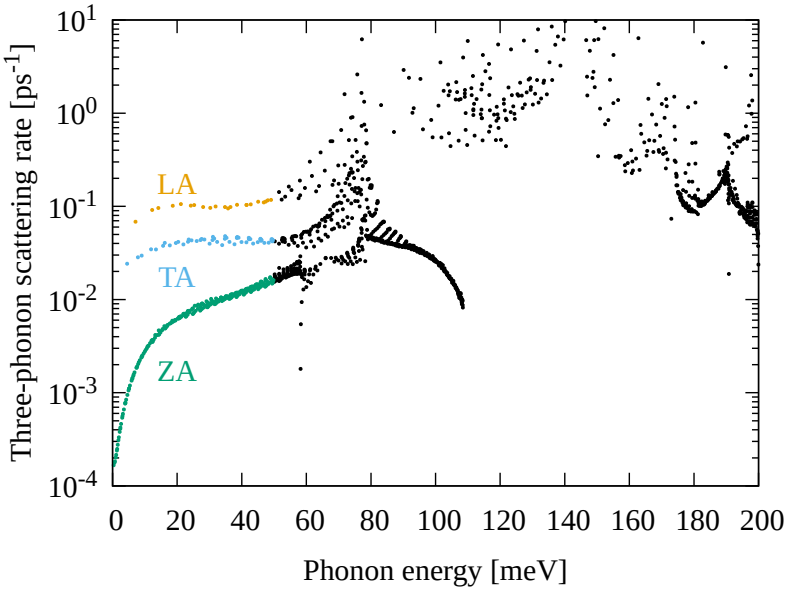


Figure 3.2: Three-phonon scattering rates of graphene. The ZA, TA, and LA modes are labeled and coloured over the 0-50 meV range.

The scattering rates of the ZA phonons are consistently much lower than the scattering rates for TA and LA phonons. This is expected because the phonon selection rules (Section 2.6) limit the number of scattering processes available to the ZA modes. The difference is much more apparent as the energies approach 0 meV. The lifetime of the lowest-energy flexural phonons are several orders of magnitude longer than the lifetime of the other modes. As we show next, these acoustic phonons play an important role in the thermal properties.

The cumulative thermal conductivity is useful for determining how the phonons at each energy range contribute to the total thermal conductivity. The cumulative thermal conductivity $\kappa_{\text{cumulative}}$ is calculated as

$$\kappa_{\text{cumulative}}(E) = \int_0^E \kappa(E')dE', \tag{3.7}$$

where $\kappa(E')$ is the contribution to the thermal conductivity from all modes in the energy range $dE'$ around energy $E'$. The cumulative thermal conductivity of graphene is shown in Figure 3.3. The converged value of the thermal conductivity was calculated to be 2740 $\mathrm{W\,m^{-1}\,K^{-1}}$. This value is in the mid-range of the values that have been determined experimentally [8, 49], and in other calculations [27, 50], with values

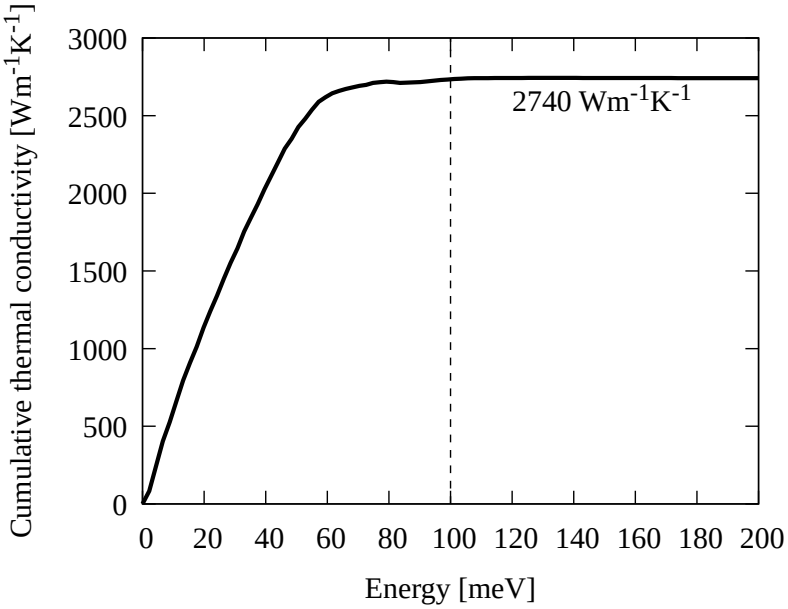


Figure 3.3: The cumulative thermal conductivity of graphene versus phonon energy. The dashed line at 100 meV shows approximately where the thermal conductivity saturates. The converged lattice thermal conductivity is 2740 $\mathrm{W\,m^{-1}\,K^{-1}}$.

ranging between 1000-5800 $\mathrm{W\,m^{-1}\,K^{-1}}$.

The cumulative thermal conductivity has a non-zero slope near zero, indicating the low-energy modes make significant contributions to the thermal conductivity. This is unsurprising because of the small scattering rates found for low-energy ZA phonon in Figure 3.2. Historically, it was thought that flexural phonons had negligible contributions to the thermal conductivity because of their low energies and velocities. However, the selection rules and finite DOS near 0meV lead to a large population of phonons with long lifetimes.

The contribution from higher energy phonons decreases steadily and finally saturates around 60 meV. This saturation occurs because 60 meV is far into the Bose-Einstein distribution where the occupation of modes is small. The contributions from energies above 100 meV are entirely negligible. Because of this, in the following sections, many of the graphs will be restricted to energies between 0 meV and 100 meV. This is to focus on the energy ranges that matter for thermal transport, the central focus of this project, and to facilitate our analysis by excluding complicated features coming from the high energy optical modes.

## 3.3 Graphite

The focus of this section is on comparing the thermal transport properties of graphite to graphene. The thermal conductivity of Equation 2.32 depends on a variety of phonon properties, each of which will be analyzed. This section is structured similarly to the previous section on graphene, beginning with the phonon dispersion and DOS, followed by the cumulative thermal conductivities, and scattering rates. The rest of the section proceeds into a more in-depth analysis of the three-phonon scattering properties, and how they each contribute to differences in the thermal conductivity of graphene and graphite.

Once again, an atomic structure relaxation was performed by minimizing the energy of the system with respect to lattice constants and atomic positions. The relaxed system was unstable at room temperature, so the quasi-harmonic approximation (QHA) was used to minimize the Helmholtz free energy at $T = 300$ K with respect to the length of the lattice vectors. The results of this calculation are in Figure 3.4. The optimized lattice parameters are $|a_1| = 2.4701$ Å and $|a_3| = 6.8718$ Å.

The phonon dispersion and DOS of graphite is shown in Figure 3.5a. The phonon dispersion of graphite has 6 more branches than graphene since it has a total of four atoms. The high-energy optical modes are degenerate throughout the BZ. The acoustic and low-lying optical modes in graphite are compared to those of graphene in Figure 3.5b.

There is a small deviation between the the ZA modes in graphite and graphene, but the LA and TA modes are nearly identical. The three low-lying optical modes, labelled with primes, become degenerate with their associated acoustic modes for long wavelengths. There is a very small deviation in the LO' and TO' modes from the LA and TA branches respectively near the $\Gamma$ point, but the ZO' branch is separated from the ZA branch throughout most of the BZ.

The flexural optical mode (ZO') corresponds to modes where the two layers of carbon atoms oscillate towards and away from each other (see Figure 3.6a). The other two low-energy optical modes, LO' and TO', correspond to the layers sliding against one another (see Figure 3.6b). The energies involved in these motions at long wavelengths ($\boldsymbol{q} \approx \boldsymbol{0}$) come primarily from inter-layer interactions since they are

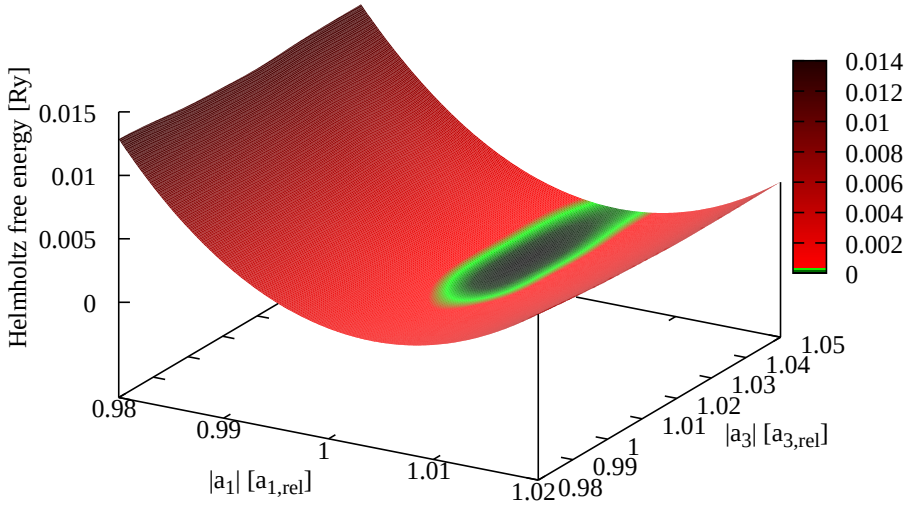


Figure 3.4: The Helmholtz free energy of graphite for different lengths of in-plane, $a_1$, and cross-plane, $a_3$, lattice vectors. The relaxed parameters were $|a_1| = 2.47$Å and $|a_3| = 6.87$Å.

essentially translations of the graphene sheets. This explains why the ZO' phonons have higher energies than the the LO' and TO' near the $\Gamma$ point: it is energetically easier to slide the sheets to the side compared to pushing them towards each other.

For the stretched graphite cases in the following section, it is expected that the energies of these modes should decrease as the inter-layer separation increases. This softening of modes should occur since they are dominated by inter-layer interactions at long wavelengths. The rest of the modes are expected to remain the same, since they are dominated in intra-layer interactions.

The DOS for graphite is nearly identical to graphene, except for at the lowest energy ranges. It is predicted theoretically that the DOS of a parabolic energy band in a two-dimensional material like graphene is constant, and the DOS is linear in $E$ for linear bands. Meanwhile, in a three-dimensional material like graphite, parabolic band results in a DOS that is proportional to $\sqrt{E}$, and linear bands contribute a DOS that is proportional to $E^2$ [34].

The DOS of graphite in Figure 3.5a appears mostly quadratic, indicating that

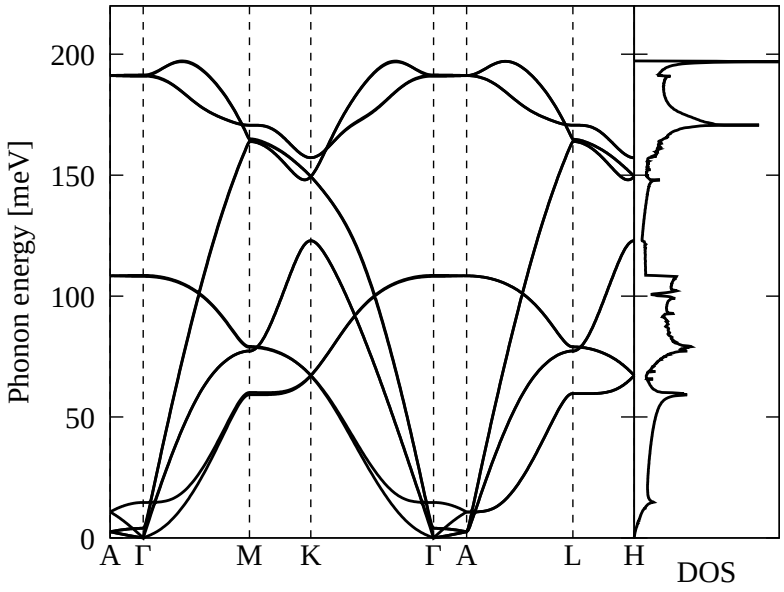


(a)

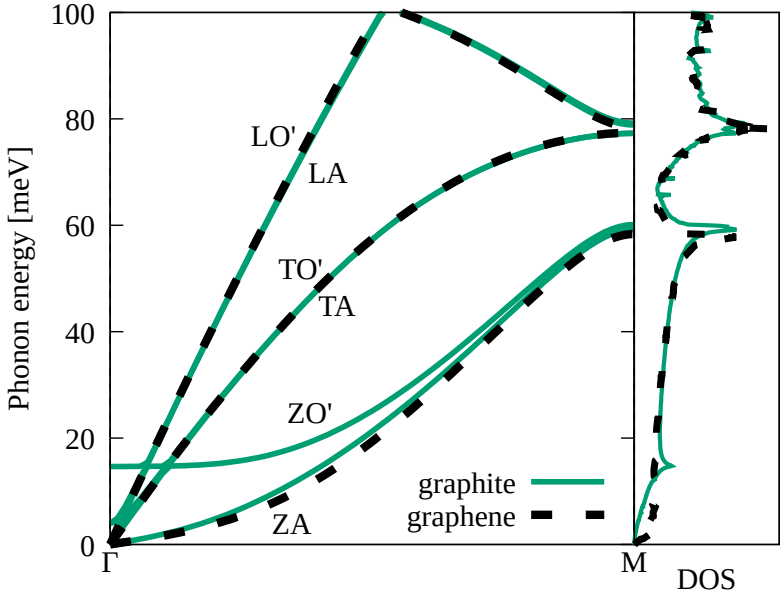


(b)

Figure 3.5: a) The phonon dispersion and DOS of graphite, and b) an enhanced comparison of the low-energy phonon modes and DOS between graphite (solid green) and graphene (dashed black).

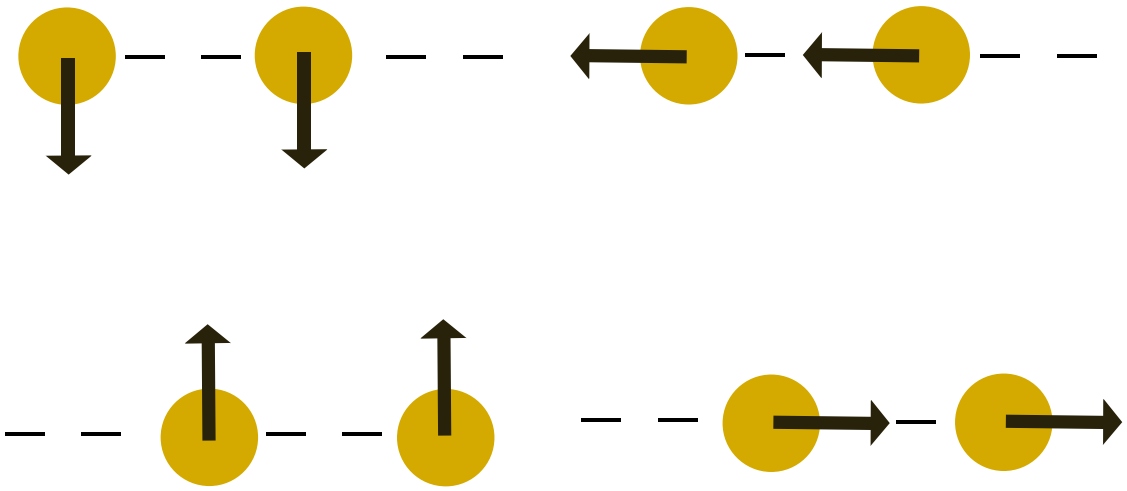

(a) (b)

Figure 3.6: Visualization of the (a) ZO' modes, and (b) TO' and LO' modes in graphite. The four circles represent the four carbon atoms in the primitive cell, and the arrows represent the direction of their movement at some point in time. The primed optical modes correspond modes where the motion of the adjacent graphene sheets are out of phase with one another.

the ZA mode may be more linear than parabolic close to 0 meV. The occupation of phonons in near-equilibrium conditions should deviate only slightly from the Bose-Einstein distribution, which behaves like $k_B T/E$ as $E \to 0$.

The difference in the shape of the DOS means that the population of low-energy phonons in graphene will be much larger than in graphite. From Equation 2.32, having a non-zero DOS around 0 meV means that there should be a large contribution to the thermal conductivity at low energies. In graphite, there are fewer states to contribute to the conductivity until higher energies, so only energy ranges with a significant DOS will contribute.

Next, the thermal conductivity of graphite was calculated using ShengBTE. The cumulative lattice thermal conductivity for graphene and graphite is shown in Figure 3.7a, along with a plot of the difference of the cumulative thermal conductivity of graphene and graphite in Figure 3.7b. The converged lattice thermal conductivity of 2050 $\mathrm{W\,m^{-1}\,K^{-1}}$ is in excellent agreement with previous experiment (1950 $\mathrm{W\,m^{-1}\,K^{-1}}$) [20] and calculations [51].

There is a large difference in thermal conductivity contribution in graphite compared to graphene in the energy range of 0 meV to 20 meV. This is likely due to the relatively large DOS in graphene, and therefore the large population of flexural phonons, compared to graphite. However, the conductivity also depends on the phonon scattering rates through $\boldsymbol{F}$ in Equation 2.32, which are expected to be lower in graphene because of the phonon selection rules described in Section 2.6. At this point in the discussion it is not yet clear from these results whether the large contributions are due to the increased DOS in graphene or form a difference in selection rules.

The cross-plane thermal conductivity in Figure 3.8 saturates at a much lower energy than the in-plane thermal conductivity, to a value of 6.7 $\mathrm{W\,m^{-1}\,K^{-1}}$, which is much lower than the in-plane thermal conductivity. The convergence at low energies is likely because the phonon dispersion in the cross-plane direction (between $\Gamma$ and $A$) is quite flat for energies above 20 meV, leading to low phonon velocities. This is in contrast to the reason behind the saturation in the in-plane direction, which was a result of the negligible occupation number for modes above 60 meV.

The scattering rates for graphite and graphene are shown in Figure 3.9. Each point

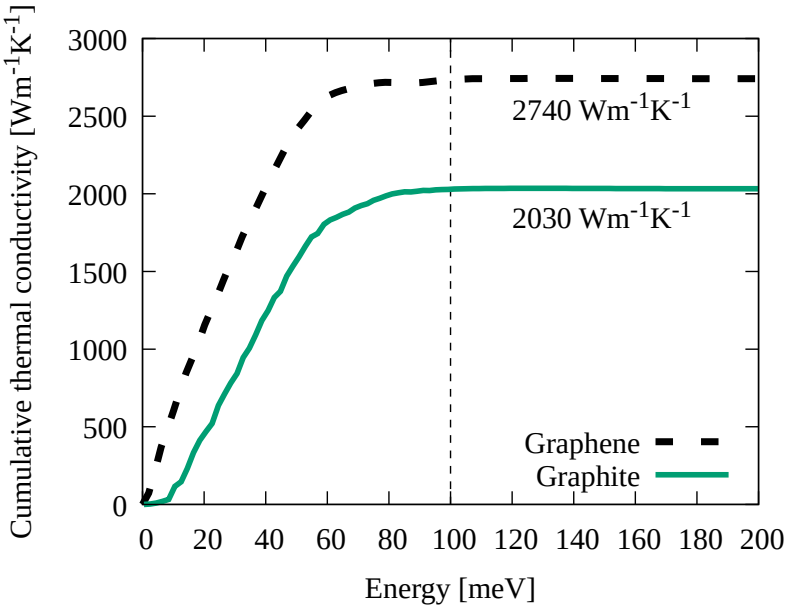


(a)

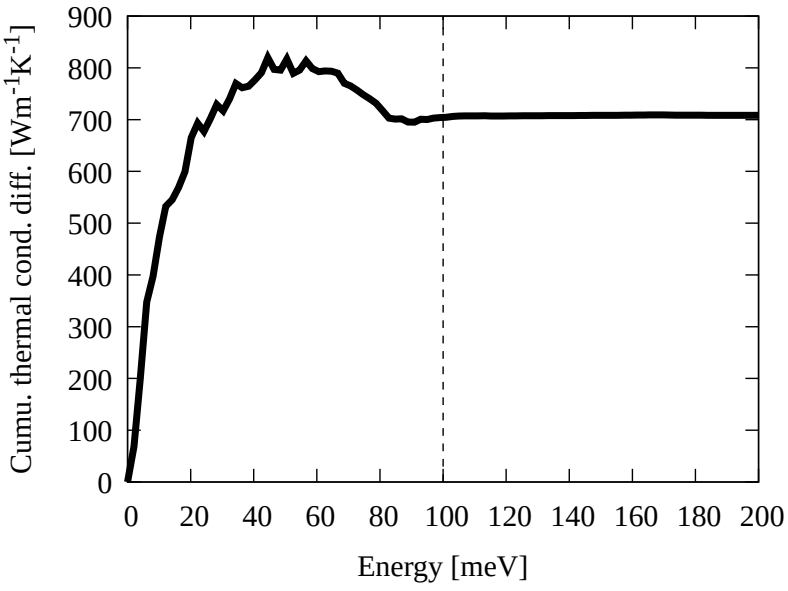


(b)

Figure 3.7: (a) The cumulative in-plane thermal conductivity for graphene (solid green) and graphite (dashed black). The converged value for graphite is 2030 $\mathrm{W\,m^{-1}\,K^{-1}}$. (b) The difference in the cumulative thermal conductivity between graphene and graphite at each energy.

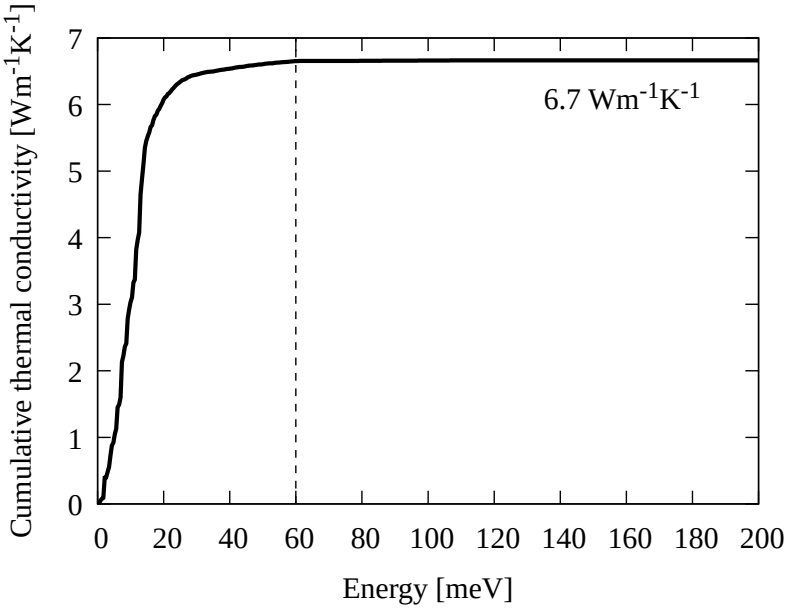


Figure 3.8: The cumulative cross-plane thermal conductivity for graphite. The converged value is 6.7 $\mathrm{W\,m^{-1}\,K^{-1}}$.

corresponds to a phonon state $(\boldsymbol{q}, p)$. There is a large spread of points below 20 meV in the three-phonon scattering rates in graphite that does not appear in graphene. These new points correspond to modes with wavevectors that have z-components, which will be elaborated on below in the discussion of phonon velocities. These only appear in graphite since it is a three-dimensional material, with a three dimensional BZ, while graphene is only two-dimensional.

The overall trend in the scattering rates are quite similar between the two materials. The scattering rates of the ZA mode are similar in both materials, but graphene appears to drop a bit more sharply below a few meV. This is strange, because it is expected that the scattering rate of flexural phonons in graphite should be much lower than those in graphene, due to the lack of selection rules. This also cannot entirely explain why the low-energy modes of graphene contribute up to 15 times more to the thermal conductivity than the same energy ranges in graphite. In order to explain the difference, a more thorough analysis of the phonon properties is required.

One important property that the lattice thermal conductivity depends on is the velocities of the phonons. The phonon velocities were calculated by ShengBTE by simply taking the derivative of the phonon energies obtained in the dispersion by the wavevector $\boldsymbol{v}_p(\boldsymbol{q}) = \boldsymbol{\nabla}_{\boldsymbol{q}}\omega_p(\boldsymbol{q})$. The in-plane velocities for graphene and graphite are

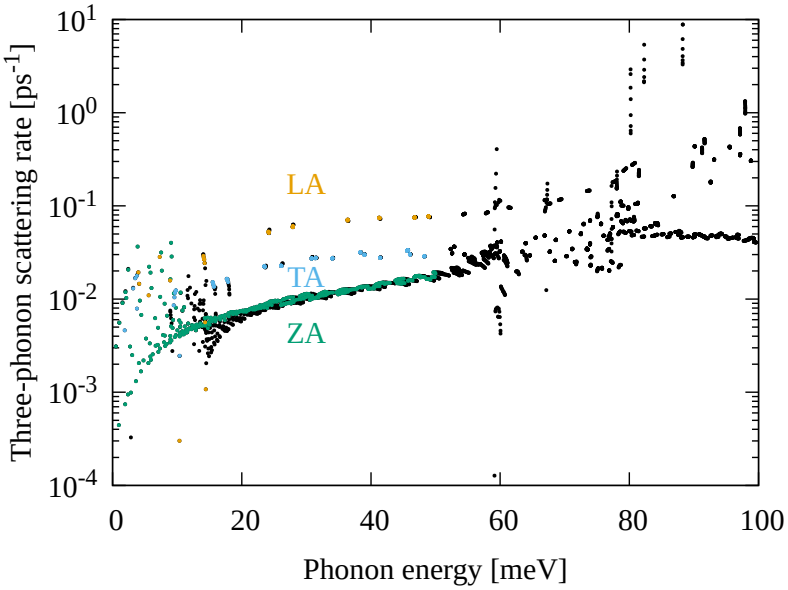


(a)

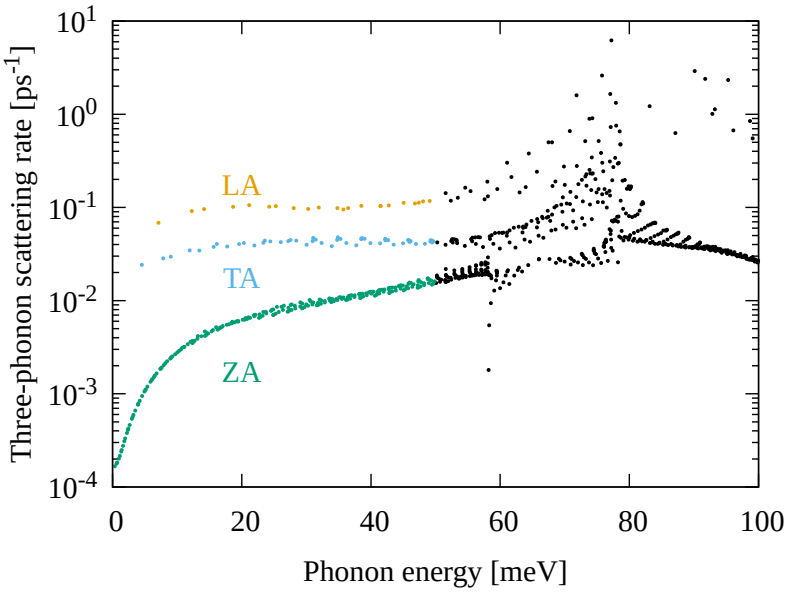


(b)

Figure 3.9: The converged three-phonon scattering rates for (a) graphite and (b) graphene. The scattering rates were calculated using a 30x30x12 $q$-grid for graphite, and a 60x60x1 $q$-grid for graphene. The acoustic modes are labelled and coloured: LA (yellow), TA (blue), and ZA (green).

shown in Figure 3.10.

The magnitude of the in-plane velocities of the flexural acoustic modes in graphite are nearly identical to the ZA velocities in graphene. Just like in the scattering rates, there is a large spread of points in the low-energy range in graphite that does not appear in graphene. Once again, this is due to the extra dimension in graphite. Figure 3.11 emphasises this by showing a plot of the phonon dispersion parallel to the axis going from Γ to M in the BZ for different values of $q_z$. $q_z$ is the $z$ component of the phonon wavevector $\boldsymbol{q}$, where $q_z = 0.180$ are wavevectors that lie on the top surface of the BZ. $q_z$ is in units of $2\pi/a$ where $a$ is the lattice constant. The ZA and ZO' modes 'fan out' to higher and lower energies respectively for values for $q_z$. This 'fanning out' of the branches through the BZ leads to the spread of the velocities and scattering rates at low energies.

It is clear from Figures 3.10a and 3.11 that the spread of velocities in the former is due to the 'fanning out' of branches in the latter. The spread of energies at the Γ point is between 0 meV and 15 meV. The branches also flatten out at the Γ point, leading to the 0 $\mathrm{km\,s^{-1}}$ in-plane speeds spread over the 0-15 meV range seen in Figure 3.10a. For longer phonon wavevectors, the energy range between the ZO' and ZA branches decreases and the slopes of each branch are more similar, leading to the decrease in the spread of velocities near ZA as energy increases in Figure 3.10a.

The fanning and flattening of the ZA branch acts to reduce the in-plane lattice thermal conductivity in two ways. First, the fannning reduces the occupation of flexural phonons since the spread of the ZA branches to higher energies reduces the occupation number from the Bose-Einstein distribution for those branches. Second, the flattening of branches lowers the velocity of the phonons, which reduces the contribution to the thermal conductivity from each phonon mode through Equation 2.32.

The speeds of phonons in the cross-plane direction are shown in Figure 3.12. The cross-plane speeds are generally much lower than the in-plane speeds, which is expected due to the weak inter-layer coupling. This is the reason why the thermal conductivity is so much lower in the cross-plane direction. The maximum cross-plane

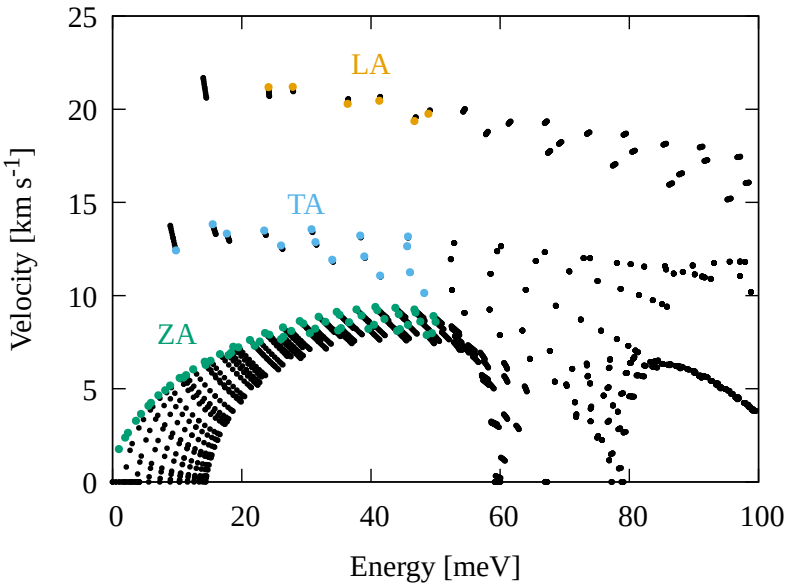


(a)

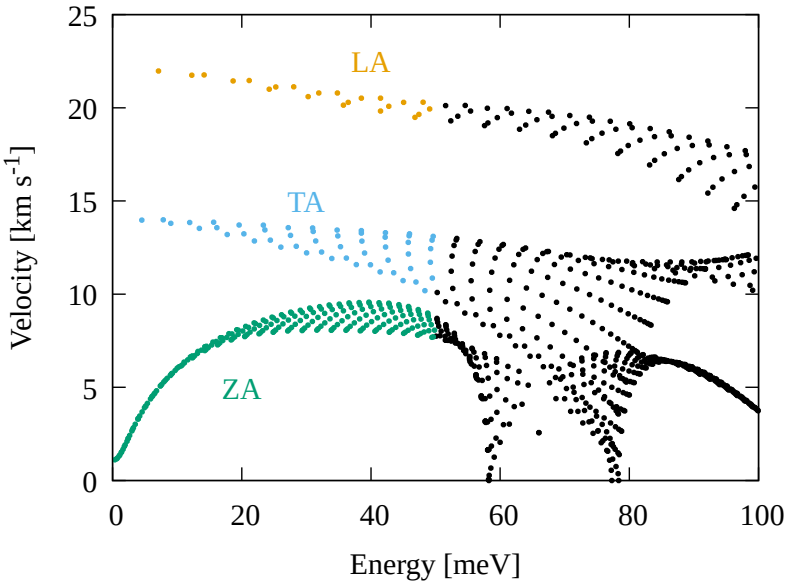


(b)

Figure 3.10: Magnitudes of the in-plane phonon velocities for a) graphite and b) graphene.

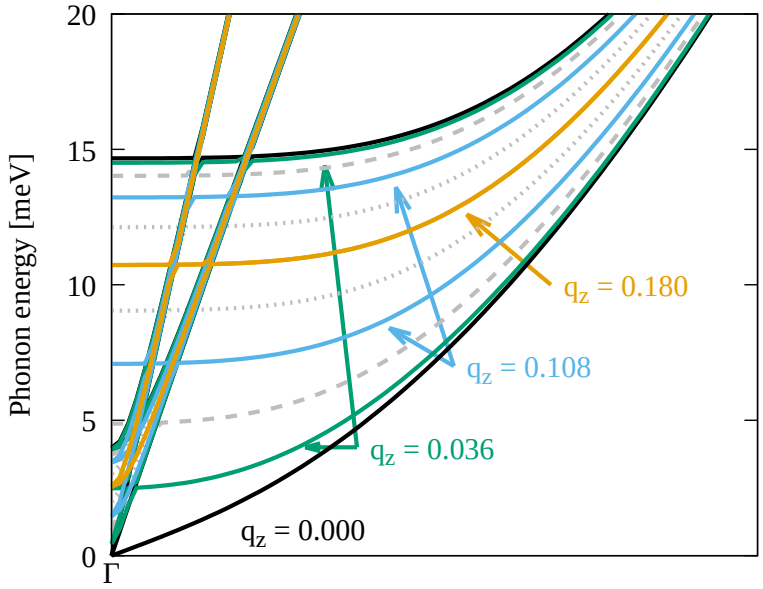


Figure 3.11: Phonon dispersion of graphite plotted parallel to the Γ to M axis with different values of $q_z$. Some of the ZA and ZO' branches are coloured and labeled, with two extra grey dashed and dotted lines corresponding to $q_z = 0.0719$ and $q_z = 0.144$ respectively to fill in the gaps.

velocities are generally smaller than the in-plane velocities and see a significant decrease over the first 20 meV. This, coupled with the decreasing Bose-Einstein distribution with energy leads to a quick saturation of the cumulative thermal conductivity with energy. This is in contrast to the in-plane direction, where the reason for the negligible contributions to $\kappa$ at high energies is solely due to the negligible occupation number.

The change in the distribution of phonon velocities should account for a decrease in the thermal conductivity between graphene and graphite, but it is only one of the factors in the thermal conductivity Equation 2.32. It also depends on the scattering properties through $\boldsymbol{F}$. In order to obtain a deeper understanding of the differences in thermal transport between graphene and graphite, each component that factors into the three-phonon scattering rates should be analyzed. One of the properties that is output by ShengBTE is the weighted phase space for three-phonon scattering processes ($W_\lambda^\pm$), which is defined as

$$W_\lambda^\pm = \frac{1}{2N_q} \sum_{\lambda'\lambda''} \begin{Bmatrix} 2(f_{\lambda'} - f_{\lambda''}) \\ f_{\lambda'} + f_{\lambda''} + 1 \end{Bmatrix} \frac{\delta(\omega_\lambda \pm \omega_{\lambda'} - \omega_{\lambda''})}{\omega_\lambda \omega_{\lambda'} \omega_{\lambda''}}. \tag{3.8}$$

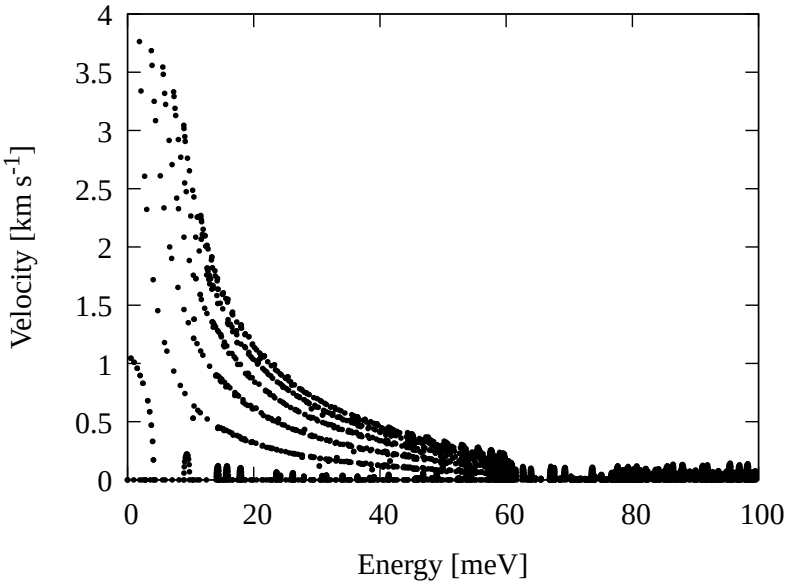


Figure 3.12: Magnitudes of the cross-plane phonon velocities for graphite.

Here, $N_q$ is the number of q points in the discretized BZ, $\lambda$ once again corresponds to the state of the phonon $(\boldsymbol{q}, p)$, and the top and bottom functions in the curly braces are taken for absorption ($W_\lambda^+$) and emission ($W_\lambda^-$) processes respectively.

The weighted phase space is similar to Equations 2.35 and 2.36 for the scattering rates, except the three-phonon scattering matrix elements are excluded. $W_\lambda^\pm$ is a useful property because it only depends on the energies and wavevectors of the phonons, which in turn depend only on the second-order IFCs. Therefore, any differences that are found in $W_\lambda^\pm$ of different materials are due only to differences in the second-order IFCs. This describes the likelihood of scattering due to states and their occupation, not the scattering potential.

In Figure 3.13 the weighted phase space of graphene is several orders of magnitude larger than those in graphite at low energies. The rest of the scatter plot appear to follow the same trend, with a few variations. In graphite (Figure 3.13a) there are two peaks at 10.7 meV and 14.7 meV. These occur where the ZO' bands flatten in the dispersion around the Γ and A point. These peaks are likely due to the flatness of the bands, since phonons in flat bands are able to scatter with many of the flat low-energy modes, like those in the ZA branch. There is also a large population of phonons at low-energies due to the Bose-Einstein distribution.

The peaks in the weighted phase space of graphene around 60 meV and 80 meV

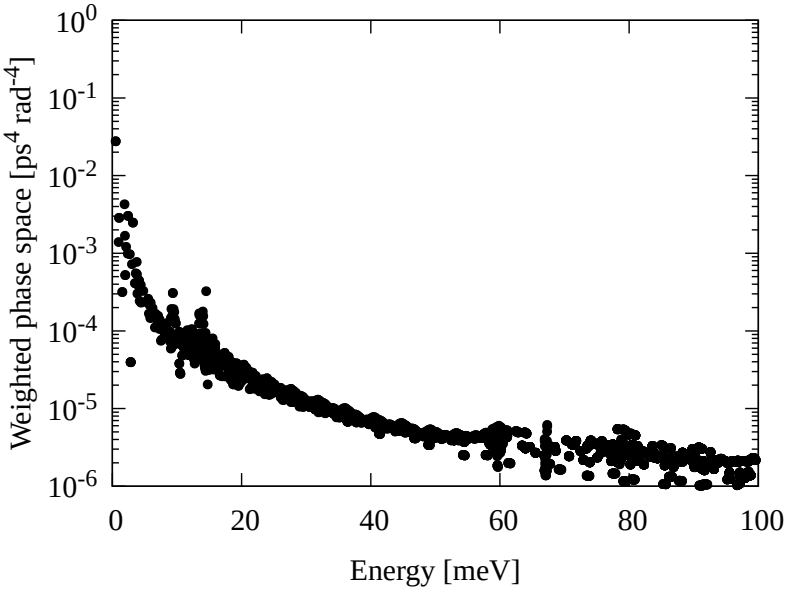


(a)

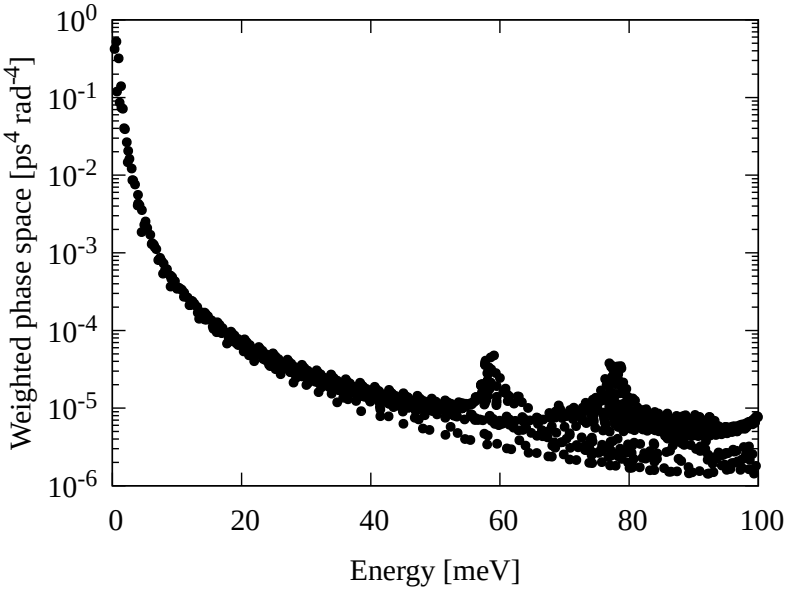


(b)

Figure 3.13: The weighted phase space for a) graphite and b) graphene.

are explained using the same reasoning. The bands are flat in those ranges, and there is an abundance of low-energy modes they can scatter with in graphene due to the constant DOS and shape of the Bose-Einstein distribution. The peaks are larger in graphene, which is probably because of the larger DOS at low energies, which leads to a much larger number of states with which the higher-energy phonons can scatter. In general, none of the peaks appear to correspond to any significant differences in the thermal conductivity, since the shape of the cumulative thermal conductivity appears constant around the energy ranges with those peaks.

The shape of the phonon dispersions of graphene and graphite (see Figure 3.5b) are similar, but the density of states is quite different due to the difference in dimensionality of the materials. The larger phonon DOS of graphene is likely why there is a larger peak in $W_\lambda^\pm$ near 0 meV. The Bose-Einstein distribution is large as well at low energies, and is independant of the material properties. The only difference between the two appears to be the DOS.

At this point in the discussion, everything except for the third-order IFCs has been analyzed. The third-order IFCs contribute to the scattering rates through the scattering matrix elements defined by Equation 2.37. These values are not explicitly given by ShengBTE, but an average of these values is obtained by dividing the three-phonon scattering rates from Equations 2.35 and 2.36 by the weighted phase space from Equation 3.8 as follows:

$$\frac{\Gamma_\lambda^\pm}{W_\lambda^\pm} = \frac{\hbar\pi}{2}\langle|V_\lambda^\pm|^2\rangle.$$

The average squared scattering potential is plotted for graphene and graphite in Figure 3.14. It was expected that the scattering matrix elements should be lower in graphene because of the phonon selection rules, but they are actually quite similar, especially for the ZA modes. In fact, the scattering matrix elements are nearly identical for ZA modes in the 0-10 meV range, which is where the largest difference in thermal conductivites occurs (see Figure 3.7b). This indicates that the third-order IFCs of graphite and graphene are probably quite similar, even though graphite does not have the same mirror symmetry seen in graphene.

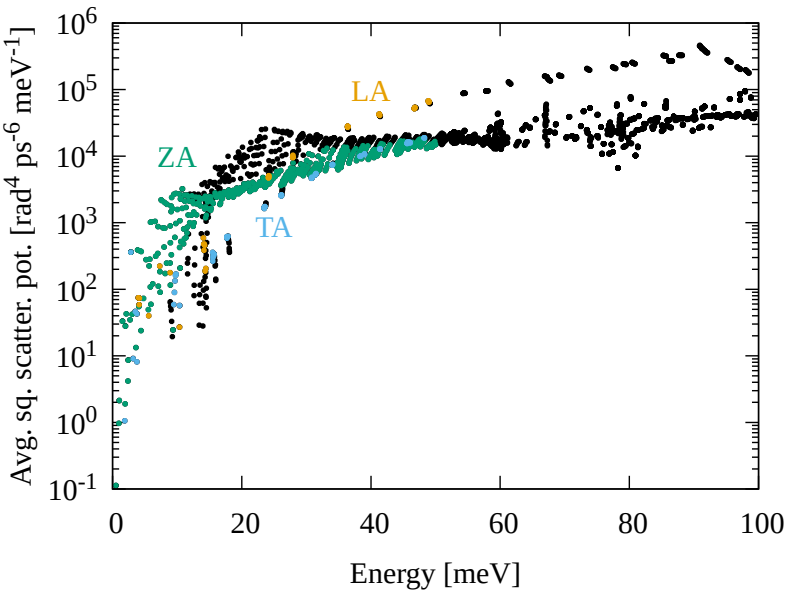


(a)

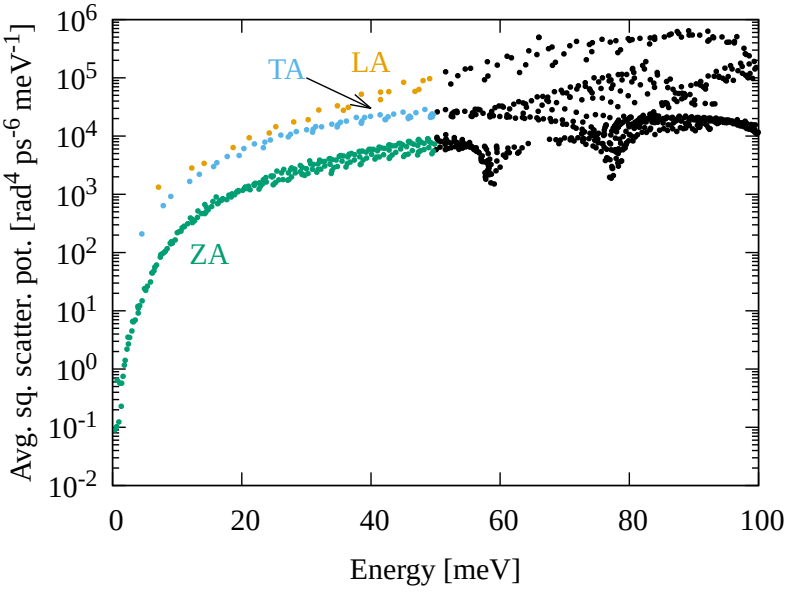


(b)

Figure 3.14: The average scattering potential for three-phonon scattering for a) graphite and b) graphene.

As a reminder, the selection rules for graphene depend on two important phonon properties, as shown in section 2.6. The first important factor is that the eigenvectors of the dynamical matrix must either be aligned with the z-axis, in the case of a flexural phonon, or be in-plane. This is true for graphene because the mirror symmetry required that the second-order IFCs with a single $z$ component must be zero, effectively decoupling the $z$ direction from $x$ and y. The second important factor is that the third-order force constants with odd numbers of $z$ components must also be 0. This leads to scattering processes with an odd number of flexural phonons being forbidden. While graphite does not have this same mirror symmetry, the following section explores how these properties are affected.

The phonon eigenvectors were obtained directly from Quantum Espresso's DFPT output. The magnitude and direction of each eigenvector was then calculated using a Python script. The angle of each eigenvector from the $x$ axis ($\theta_x$) and $z$ axis ($\theta_z$) are shown in Figure 3.15. Angles from the $y$ axis are not included because it does not add any information not already contained in the $\theta_x$ and $\theta_z$ data.

The distribution of angles for graphene (Figure 3.15b) shows quite clearly that nearly all of the eigenvectors are either directly in the $z$ direction ($\theta_z = 0°$) or perpendicular to the $z$ axis ($\theta_z = 90°$). The eigenvectors that are perpendicular to the z-axis are directed within the $xy$ plane according to the distribution of $\theta_x$. As a reminder, in graphene, the eigenvectors with $\theta_z = 0°$ correspond to the flexural phonon modes, while eigenvectors with $\theta_z = 90°$ are longitudinal or transverse. This constraint for eigenvectors to either be in- or out-of-plane is what lead to the first part of the selection rules for graphene in section 2.6, so the results are consistent with the selection rules for graphene so far.

The distribution of $\theta_z$ for graphite in Figure 3.15a is nearly identical to the distribution for graphene. Therefore, the eigenvectors are still mostly either in the z-direction, or constrained to the $xy$ plane. Because of this, it is still possible to separate them into flexural and non-flexural phonons. Flexural phonons in graphite are phonons with eigenvectors that are mostly in the $z$ direction ($\theta_z \approx 0°$), while the longitudinal and transverse are mostly in-plane ($\theta_z \approx 90°$).

This result is significant because the first requirement for the selection rule in graphene was that the phonons must be either in- or out-of-plane. In graphite, 97.3%

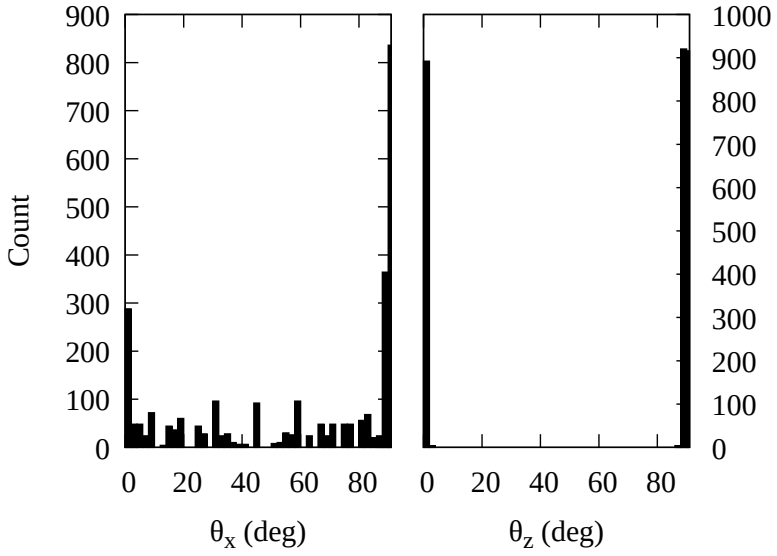


(a)

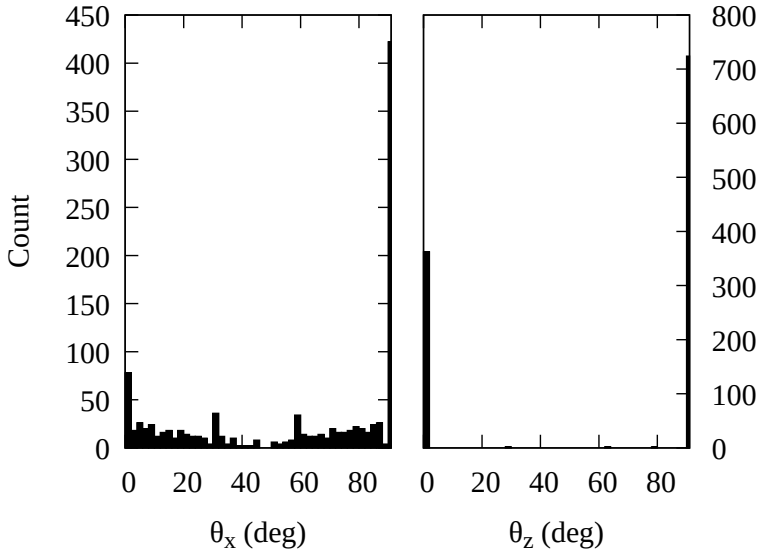


(b)

Figure 3.15: Histograms of the angle, $\theta$, of the phonon eigenvectors, $\boldsymbol{\epsilon}$, from the $x$ and $z$ axes. A binwidth of 2 ° was used. For graphite (a), 30.3% of the eigenvectors were within 0.76° of the z-axis, with an average value of 0.08°. 38.1% of those values were exactly 0°. 67.0% of the eigenvectors were within 0.75° of the $xy$ plane with an average value of 0.05°. 50.0% of them were exactly 0°. The last 2.7% were within 3° of either the $z$ axis or $xy$ plane. For graphene (b), 33.2% were exactly aligned with the z-axis, 66.3% were exactly in the $xy$ plane, and the last 0.5% were at random angles.

of the phonon eigenvectors were within 0.76° of being in- or out-of-plane, with an average angle of 0.064° from either. Therefore, the orthogonality of phonon eigenvectors that is required for the selection rules still mostly holds.

The next part of the selection rule depends on the distribution of third-order IFCs, $\Phi_{ijk}^{\alpha\beta\gamma}$, which is shown in Figure 3.16. As a reminder, the selection rules for graphene require that the third-order IFCs, $\Phi_{ijk}^{\alpha\beta\gamma}$ where $\alpha\beta\gamma$ have an odd number of $z$ components, vanish. For graphene (Figure 3.16b), the IFCs with an odd number of $z$ components were all exactly 0 eV$\text{Å}^{-3}$ This, combined with the distribution of eigenvectors above, means that the selection rules were properly reproduced for graphene. The force constants with an even number of $z$ components had a significant number of non-zero values. The force constants with no $z$ components appear to be generally be larger than those with two $z$ components, which is expected since the forces in the $z$ direction are dominated by inter-layer interactions, which are much weaker than interactions between adjacent atoms in a single layer.

In graphite (Figure 3.16a), there is a very similar trend. The third-order IFCs with an even number of $z$ components have a large range of values. For IFCs with one or three $z$ components, 60.5% were still equal to zero. The values of the remaining 39.5% were clustered very closely around zero when compared to the IFCs with even numbers of $z$ components.

It appears as though the phonon selection rules still mostly hold for graphite. Nearly half of the phonon eigenvectors are still either in- or out-of plane for graphite, and the rest are at angles that are negligible. More than half of the third-order IFCs with an odd number of $z$ components were still zero for graphite, while the remaining values were also negligible. The combination of these two factors help explain why the average squared scattering matrix elements were nearly identical for flexural phonons, despite graphite not having the same symmetry that leads to the selection rules in graphene. While many of the scattering processes that were forbidden in graphene due to the selection rules are allowed in graphite, it appears that they are improbable.

The majority of the difference between thermal transport in the two-dimensional graphene and the three-dimensional graphite appears to be a result of the change in the shape of the phonon dispersion. In graphite, the extra dimensionality of the BZ results in changes in the DOS as a result of the spreading of what were ZA modes in

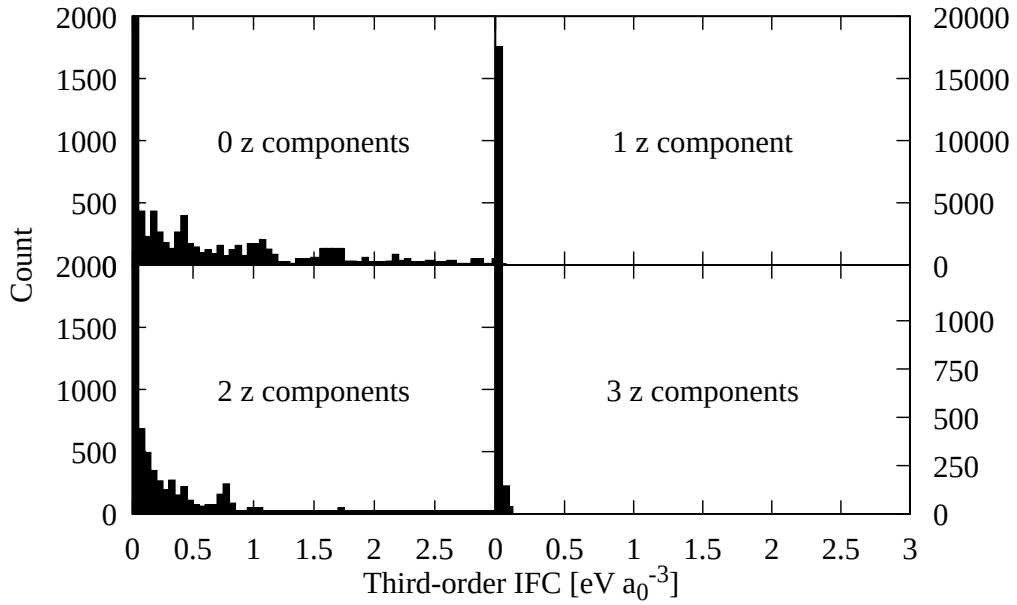


(a)

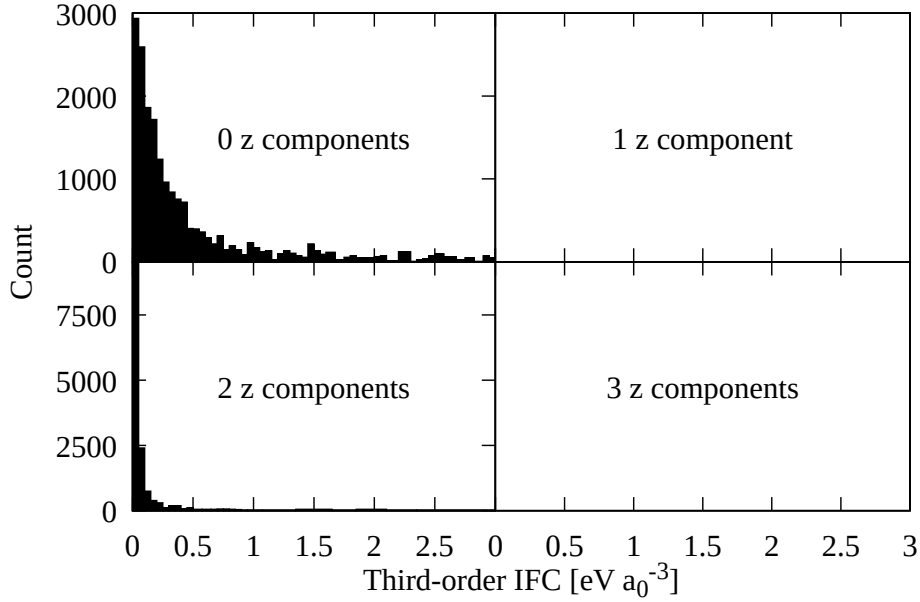


(b)

Figure 3.16: Histograms of the distribution of third-order IFCs. The bin width was 0.05eV$a_0{}^{-3}$. Each of the subplots correspond to third-order IFCs with a different number of z-components. For graphite (a), 60.8% of the IFCs with one z-component, and 57.5% of the IFCs with three z-components, were zero. For the non-zero IFCs, 95% of the values are in the range 0-3.38eV$a_0{}^{-3}$ and 0-1.7eV$a_0{}^{-3}$ for zero and two $z$ components respectively. 95% of the non-zero IFCs were between 0-0.03eV$a_0{}^{-3}$ for one $z$ component, and 0-0.1eV$a_0{}^{-3}$ for three $z$ components. For graphene (b), all of the IFCs with one and three z-components were exactly zero.

graphene to higher energies, leading to lower populations of phonons. This combined with the reduction in phonon velocities appears to be the most significant difference between the phonon scattering properties in graphene and graphite. How exactly this fanning out of modes contributes to changes in the thermal conductivity is explored in the following section by observing how the phonon properties change as layers are pulled apart from each other in graphite.

## 3.4 Stretched graphite

In this section, the differences in each of the phonon properties above will be explored once again, but in the context of graphite that is strained in the $z$ direction. This straining results in a slow separation of the graphene sheets in graphite. This is to model the process of pulling the graphite layers apart until they no longer interact with one another, effectively becoming seperate graphene sheets. In this way, it is possible to analyze the transition of phonon properties from a three-dimensional material like graphite, to a two-dimensional material like graphene.

While the strained graphite cases may be non-physical, they should serve as a useful tool to observe the transition in a system that conserves symmetry. As described in Chapter 1, previous studies on 2D-to-3D transitions focus on the addition of layers, going from a single layer, to a bi-layer, tri-layer, etc. until it is essentially modelling the bulk version of the material. However, these systems do not have the same symmetries that are found in graphene and graphite. There is a mirror symmetry in the plane for graphene, and for each carbon layer in graphite. For systems with an even number of graphene layers (bi-layer, quad-layer, etc.) there are no mirror symmetry planes within any of the graphene layers. For systems with odd numbers of graphene layers (tri-layer, quintuple-layer, etc.), there is only a mirror symmetry plane for the central graphene layer.

Straining graphite in the $z$ direction until it is essentially graphene is advantageous because it conserves the mirror symmetries in graphite. It is important to maintain these mirror symmetries for each case since the selection rules for graphene depend on them. By straining the graphite in the z-direction by small increments between equilibrium graphite and graphene, there should be a slow, continuous change in the IFCs, which will appear in as changes in the phonon properties change when going

from graphene to graphite. This is opposed to the sudden symmetry breaking that occurs by adding extra layers to graphene.

This section begins once again by looking at the phonon dispersions and DOS for each of the cases, followed by the scattering rates and cumulative thermal conductivity. The rest of the phonon properties found in the section for graphite were still calculated in each case, but some were not particularly useful for the discussion and are omitted.

The transition of the thermal properties between graphene and graphite was quite smooth, and only two values of strained graphite were really required to understand what is happening through the transition. The values chosen were a strain in the $z$ direction of 1.05 and 1.10, where the strain is defined as $a_3/a_3^0$, where $a_3$ is the length of the lattice vector in the $z$ direction, and $a_3^0$ is the value of the same vector for equilibrium graphite. The in-plane lattice vectors were unaltered during the stretching. As a reminder, the parameters used in the calculations for the strained graphite cases were identical to the converged parameters used for graphite above for all calculations.

The phonon dispersions and DOS for each case are shown in Figure 3.17. This time, they are split up by modes in order to emphasize the differences between the individual modes. The acoustic modes for graphite and the strained cases are ignored because they are identical to the acoustic modes for graphene, which are shown as well as dashed black lines. The low-lying optical modes are where all of the interesting differences in the phonon dispersions occur.

For the lowest flexural optical modes, ZO', there is a clear softening of the branch as the graphite is strained. This is what was expected since the flexural optical modes correspond to adjacent sheets oscillating along the $z$ direction (see Figure 3.6a). This type of motion is dominated by inter-layer interactions. The distance between layers increases as graphite is strained, leading to a reduction in the strength of the interlayer interaction, and a corresponding reduction in the energy of the ZO' branch.

There is a peak in the DOS for the graphite cases where the ZO' branches flatten out at the $\Gamma$ point. The softening of these branches leads to a reduction in the energy where the peak in the DOS is found. This is important since the number of states available to transport heat plays an important role in the thermal conductivity. The

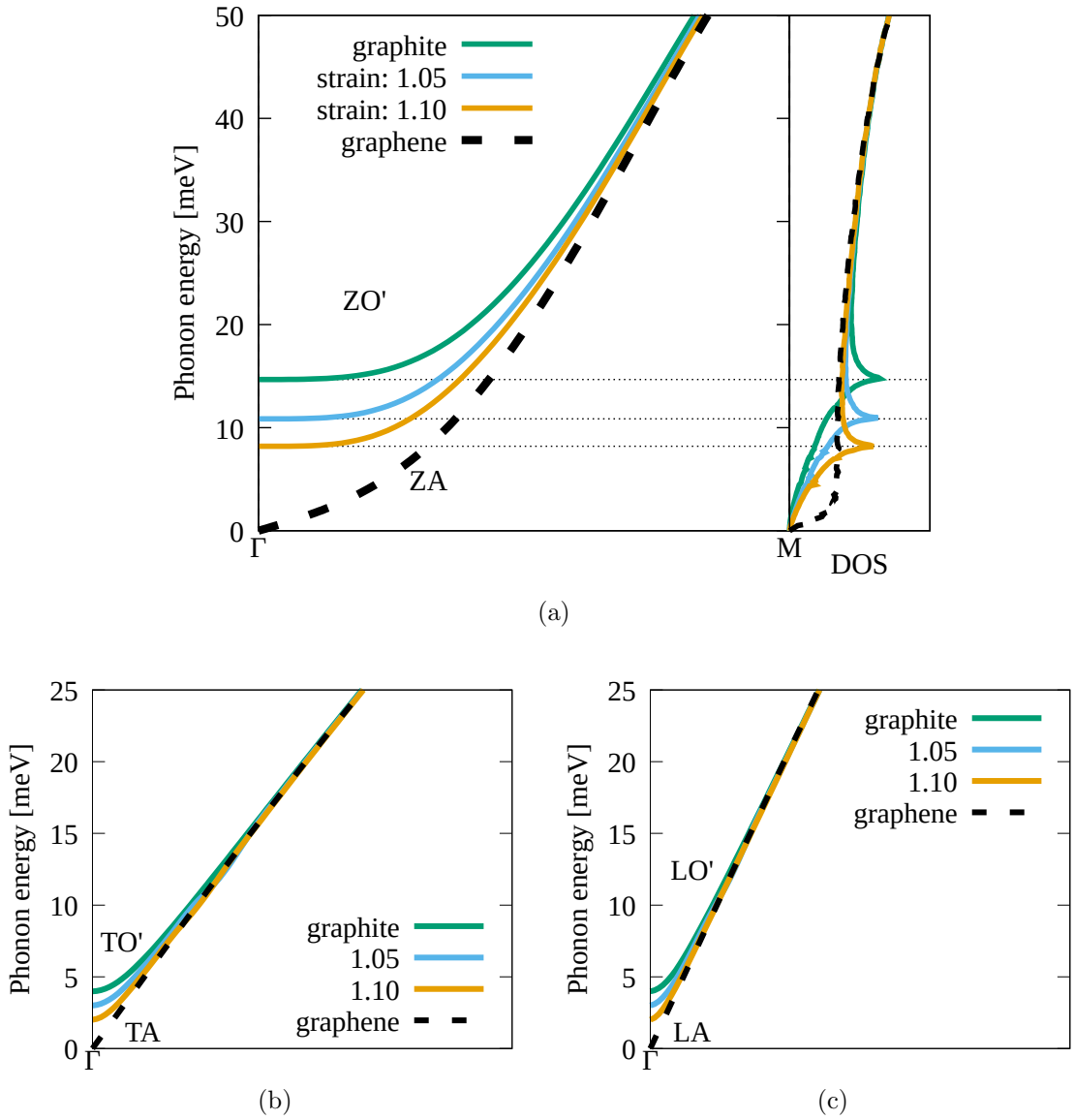


Figure 3.17: Enhanced phonon dispersions for the low-lying optical modes along $\Gamma \rightarrow M$, (a) ZO', (b) TO', and (c) LO', in graphite and each stretched case. Each plot also contains the associated acoustic phonon modes in graphene. The black dotted lines in (a) are to highlight that the peak in the DOS corresponds to the flattening of the ZO' mode at the $\Gamma$ point.

reduction of the energy of the peak in the DOS means that the large number of states from the ZO' mode will have higher occupation numbers through the Bose-Einstein distribution. A large number of states with a large occupation number tends to increase the thermal conductivity. This peak moves down in energy as the layers are pulled apart, eventually becoming a constant DOS in graphene.

The same softening of the modes is seen in the TO' and LO' branches as well near the $\Gamma$ point. In this case, the peaks in the DOS corresponding to these modes are negligible, so it is not expected that their softening contributes much to the increase in the thermal conductivity. In general it appears that increasing the seperation between layers leads to a softening of these bands. Eventually, each of the low-lying optical branches becomes degenerate with their associated acoustic branch in graphene for all wavevectors.

The softening of the ZO' modes is also important because of the scattering rates of the ZO' modes. A comparison of the scattering rates for each of the cases in shown in Figure 3.18. The scattering rates for all of the modes are nearly identical in this case, except for the low-energy phonon modes. The ZO' in particular have scattering rates that are significantly lower than most of the other phonons, which is seen as the dip in the scattering rates around 15 meV in graphite. This dip in the scattering rates moves towards lower energies as graphite is stretched. This means that the ZO' modes have long lifetimes as well as low energies, leading to a large population of long-lived phonons. The ZO' branch eventually becomes the ZA branch in graphene, and still retains much of its properties.

To see how the change in the ZO' modes affect the thermal conductivity, it is instructive to look at the cumulative thermal conductivity for each case. The converged lattice thermal conductivites follow the expected pattern of increasing as graphite is strained towards graphene. The shape is quite similar in each of the cases, but the contribution to the thermal conductivity of the low-energy modes gets significantly larger as graphite is strained. Looking at the differences in the cumulative thermal conductivities in each case, most of the difference occurs between 0 and 40 meV. The steepest slopes (i.e. largest contributions) occur in the 10-20 meV range for the strained cases, which is around where the ZO' modes softened to at the $\Gamma$ point. There is still a significant difference between the contributions from the strained cases

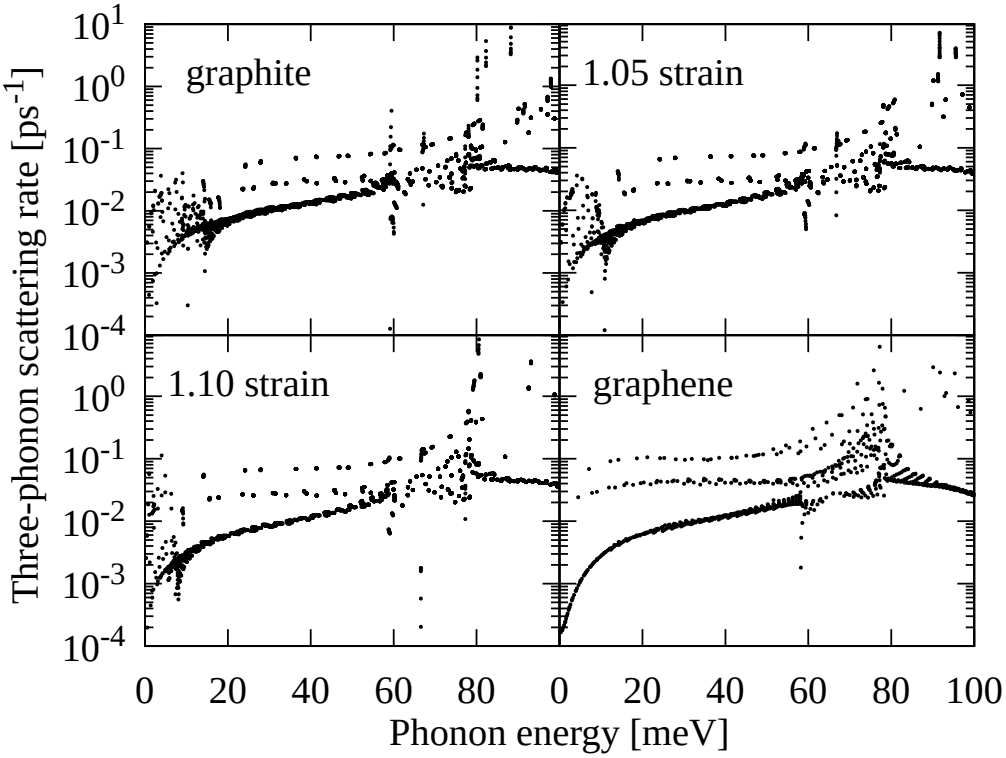


Figure 3.18: The converged three-phonon scattering rates for the cases of graphite, 1.05 strained graphite, 1.10 strained graphite, and graphene. Each point on the scatter plot represents a phonon in one state.

that can not only be due to the softened modes.

There is a change in the shape of the ZO' branches as well for strained graphite in Figure 3.17. For graphite, the ZO' branch is very flat at Γ, but as it is strained it gets steeper, approaching the slope of the ZA band. The phonon velocities depend on the derivative of the energy with respect to the wavevector, so a steeper slope results in faster phonons. This is seen in Figure 3.20. For strained graphite, there is still a fanning out of flexural modes between the ZA and ZO' branches. The fanning becomes more condensed as the strain is increased, becoming more like the ZA modes in graphene. On average, this leads to an increase in the velocites of the modes between the ZA and ZO' branches. The contribution from a single mode to the thermal conductivity depends on the squared speed, so any change in the phonon speed can be significant.

The cross-plane phonon velocities also behave generally as expected for the strained cases. There is a significant decrease in the phonon speeds as graphite is strained, eventually all the of cross-plane speeds would become 0, like in graphene where there is no cross-plane transport.

Finally, it is important to see how the IFCs changed in order to see if the phonon selection rules apply. If the second-order IFCs change much between systems, it would be seen as a change in the phonon dispersion and eigenvectors. The selection rules depend on the second-order IFCs through the orientations of the phonon eigenvectors. From Figures 3.22 and 3.23, it appears as though there is very little, if any, difference between the orientations of the eigenvectors in graphite (see Figure 3.15a), 1.05 strained graphite, and 1.10 strained graphite. They still are all either entirely or mostly oriented in the $z$ direction or within the $xy$ plane.

The final important component of the selection rules is the values of the third-order IFCs. Comparisons of their distributions for each case are shown in Figures 3.24, and 3.25. This time there is a focus on a smaller energy range than in the previous section, to try to emphasize any small changes in the IFCs. Also, only the IFCs with an odd number of $z$ components are included since they are the important ones for the phonon selection rules.

Beginning with the third-order IFCs with a single $z$ component, it appears as the values get progressively smaller as graphite is strained. The difference is small, but

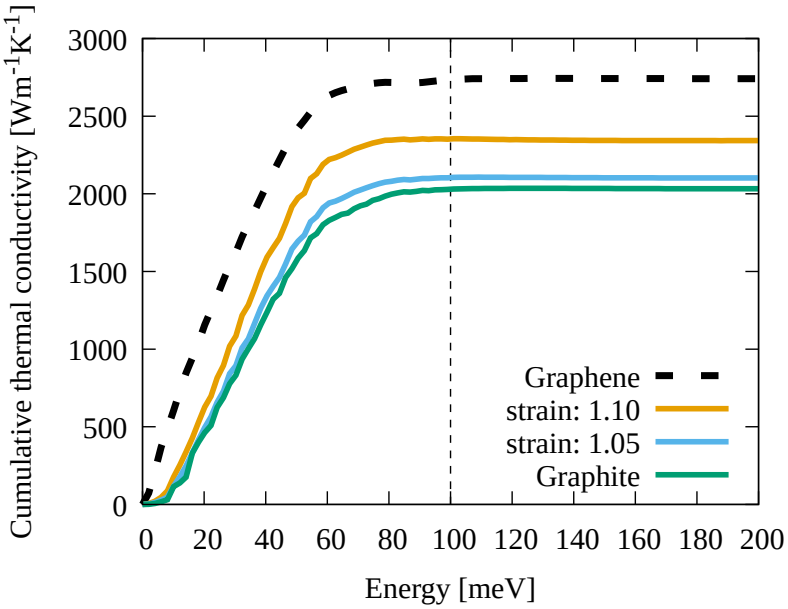


(a)

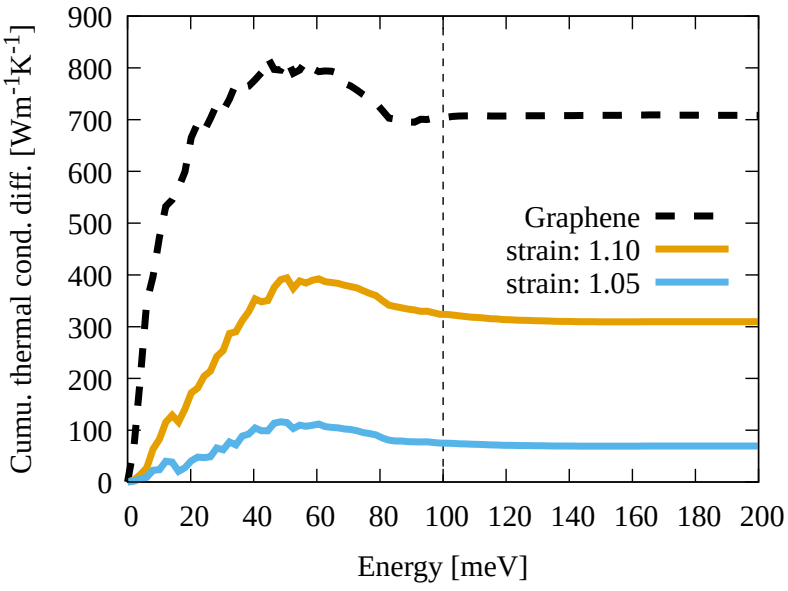


(b)

Figure 3.19: (a) Comparison on the cumulative thermal conductivity for the cases of graphite (green solid), 1.05 strained graphite (blue solid), 1.10 strained graphite (yellow solid), and graphene (black dashed). (b) The difference between the cumulative thermal conductivites of the strained cases and graphene when compared to graphite.

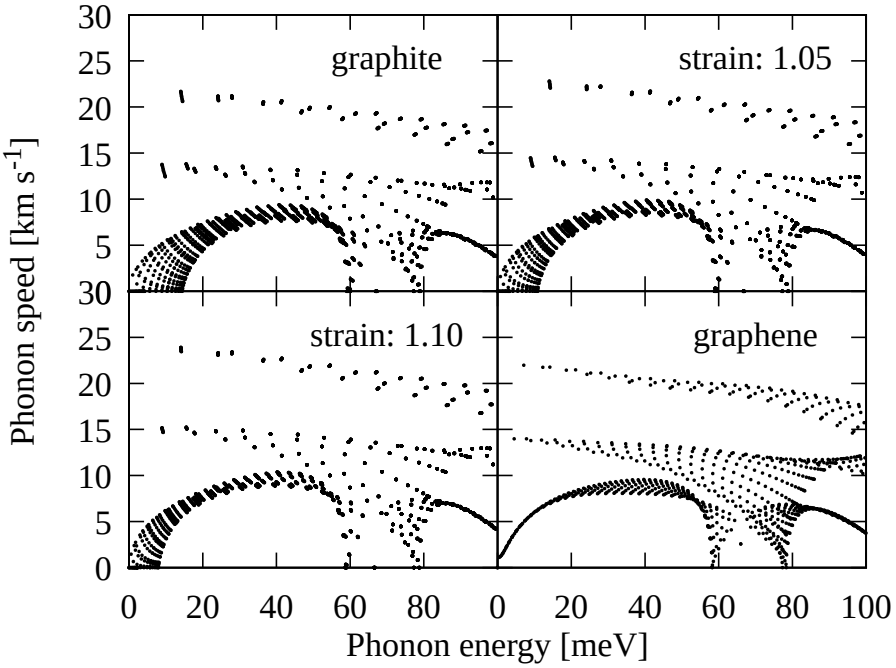


Figure 3.20: Comparison of the in-plane phonon velocities for the cases of graphite (top left), 1.05 strained graphite (top right), 1.10 strained graphite (bottom left), and graphene (bottom right).

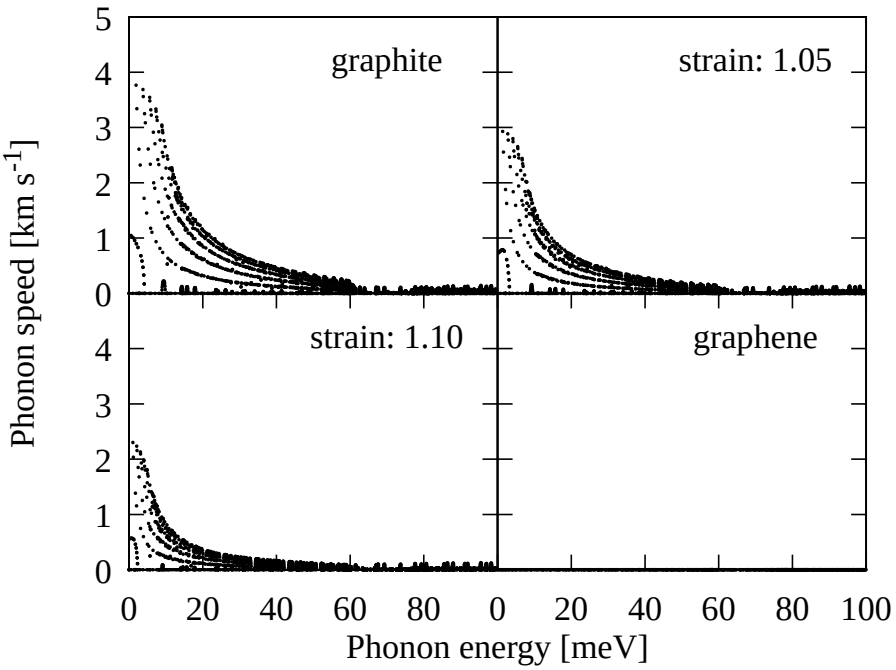


Figure 3.21: Comparison of the cross-plane phonon velocities for the cases of graphite (top left), 1.05 strained graphite (top right), 1.10 strained graphite (bottom left), and graphene (bottom right).

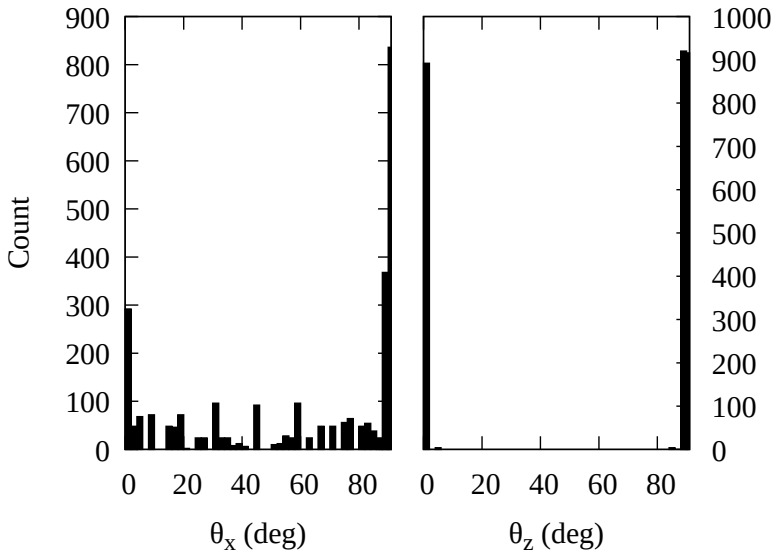


Figure 3.22: The angles of the phonon eigenvectors from the $x$ and $z$ axes for graphite that is strained along the $z$ direction by 1.05.

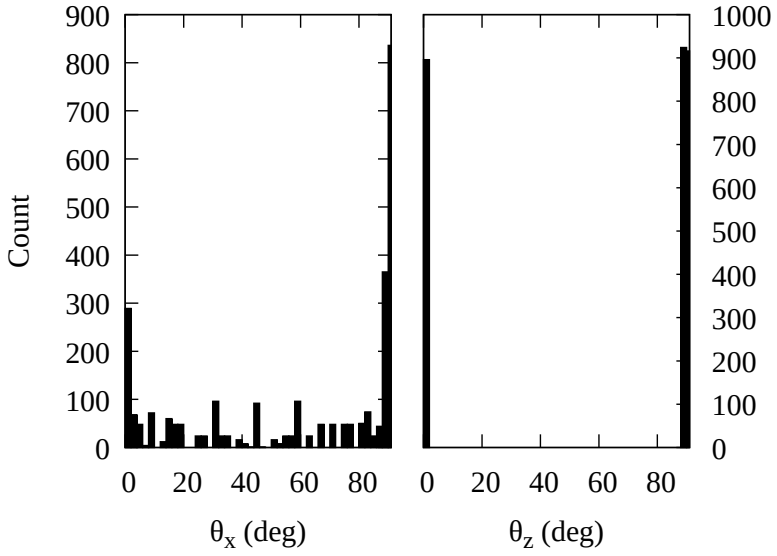


Figure 3.23: The angles of the phonon eigenvectors from the $x$ and $z$ axes for graphite that is strained along the $z$ direction by 1.10.

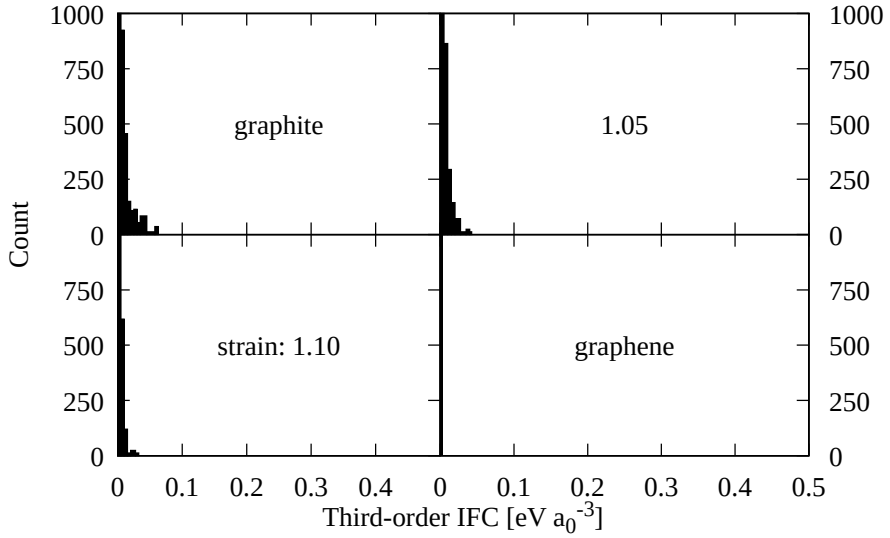


Figure 3.24: Comparison of the third-order IFCs with a single $z$ component for the cases of graphite (top left), 1.05 strained graphite (top right), 1.10 strained graphite (bottom left), and graphene (bottom right).

smaller third-order IFCs will lead to lower scattering rates. For the IFCs with three $z$ components, the change between the graphite and strained cases is even smaller. Once again it is expected that these would decrease since they are dominated by inter-layer interactions, but the difference is so small that its unlikely that it would change the overall thermal conductivity in a significant way.

Lastly, it is noted that the properties for stretched graphite beyond 1.10 were not calculated because they appeard to be entirely unstable, likely prefering to form bilayers, and leading in negative phonon frequencies.

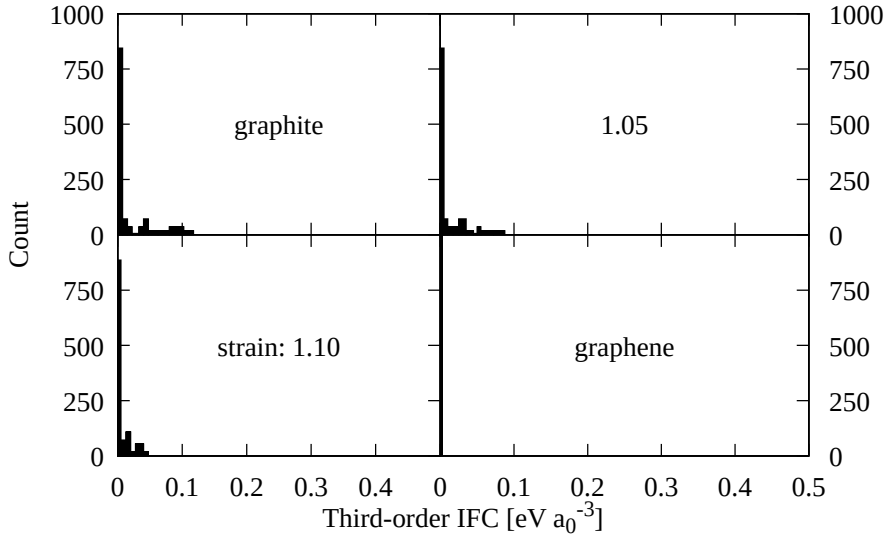


Figure 3.25: Comparison of the third-order IFCs with three $z$ components for the cases of graphite (top left), 1.05 strained graphite (top right), 1.10 strained graphite (bottom left), and graphene (bottom right).

# Chapter 4

# Conclusion

Two-dimensional materials have exceptional properties, and are often derived from their layered bulk counterparts. The bulk form tends to retain some of the characteristics of their monolayer form. Studies often focus on either limit, but little is known about the mechanism behind how the properties transition from 3D to 2Ds. The purpose of this study was to observe how the thermal transport properties of layered materials behave when they transition between two and three dimensions, by calculating the phonon transport properties as the layers of the bulk material were systematically pulled apart until they were effectively isolated monolayers. The transition between graphite and graphene was used, since it has a relatively simple structure and both materials have been extensively studied.

All of the properties of the materials were calculated from first principles. Density functional theory (DFT) was used to calculate the interatomic force constants (IFCs) of the material. The IFCs were then used to calculate the phonon dispersion, and the phonon scattering properties, from which the transport characteristics were calculated using iterative solutions to the Boltzmann transport equation (BTE). This method was used to investigate the thermal transport properties of graphene, graphite, and finally each of the stretched cases of graphite.

For graphene, the phonon dispersion was consistent with previous calculations and experimental results, giving rise to flexural acoustic (ZA) phonons near $q = 0$ that scale as $q^2$. The converged lattice thermal conductivity of 2740 $\mathrm{W\,m^{-1}\,K^{-1}}$ was in good agreement with both experimental measurements and computational results. In graphene, the exceptionally high thermal conductivity is attributed to certain selection rules that reduce the likelihood of three-phonon scattering for the flexural modes [25, 26]. The reduced likelihood of scattering results from a mirror symmetry that requires that certain second- and third-order IFCs vanish. The corresponding IFCs that were calculated for graphene were in fact zero, indicating that the phonon

selection rules were properly reproduced.

In the case of graphite, the phonon dispersion and DOS produced here were also consistent with previous results. The converged lattice conductivity of 2050 $\mathrm{W\,m^{-1}\,K^{-1}}$ was also in great agreement with previous measurements and calculations. Surprisingly, the properties of the IFCs that result in the selection rules for graphene were nearly entirely reproduced in graphite, indicating that the selection rules still mostly apply to graphite. The significant reduction in the thermal conductivity of graphite compared to graphene is then likely not attributed to the absence of selection rules.

The primary difference between the phonon properties of graphene and graphite appeared to be the shape of their phonon dispersions. In graphite, there is a 'fanning out' of branches between the ZA and ZO' mode which corresponds to phonon modes that have wavevectors and velocities with small cross-plane components. This is a result of it being a 3D dispersion, and is the reason why the DOS goes to zero in 3D, while it was constant in 2D. The other low-lying optical modes were degenerate with their acoustic counterparts through most of the BZ, but the ZO' modes had a large spread between ZA and ZO'. These branches also had small out-of-plane velocities and contributed to most of the cross-plane thermal transport. They were also flatter in-plane, leading to smaller in-plane velocities than the ZA modes in graphene. This fanned-out region is also where a majority of the difference in contributions to thermal conductivity between graphene and graphite occured.

The results for stretched graphite tied the phonon dispersions of the two limiting cases together nicely. The trend in the thermal conductivity of stretched graphite behaved exactly as expected, increasing from the conductivity of graphite to the conductivity of graphene as the distance between layers increased. The energy of the low-lying optical modes progressively softened as well, eventually becoming degenerate with the acoustic modes in the limiting case of graphene. The 'fanning out' of branches between ZA and ZO' became smaller as graphite was stretched since the ZO' branch approaches ZA. This results in an overall reducton in the energy of those modes, and an increase in their average velocity.

It appears that the difference in the thermal transport properties of graphene and graphite is mostly due to differences in the 3D and 2D DOS, which are a result

of the 'fanning out' of phonon branches between the ZA and ZO' branches. As the states between the ZA and ZO' branch decrease in energy when transitioning between graphite and graphene, the occupation number for each mode increases because the Bose-Einstein distribution is larger at smaller energies. The in-plane velocities of these phonons increase as well. The ZO' phonon states also have particularly long-lived phonons because of the flexural phonon selection rules, so they contribute a large amount to the thermal conductivity in graphite. As graphite is stretched, these modes move to lower energies and contribute even more to the thermal conductivity because of their increase in occupation number and speed.

The fanning-out of modes is due to the cross-plane interactions, which causes modes that would normally correspond to acoustic modes in the monolayer form of the material to spread out to higher energies. Some other materials that have flexural acoustic modes in the monolayer form and ZA and ZO' modes in the bulk are $MoS_2$ and $WS_2$ [21]. They also have the characteristic peak in DOS where the ZO' meets the $\Gamma$ point, indicating that the shape of the ZO' bands are flat like those in graphene. Due to these similarities in the phonon dispersion, these materials would be a good next step for applying this analysis to determine if this mechanism is the cause of the differences in thermal conductivites for other layered materials.

It is also important to note that the exceptionally high thermal conductivity of graphene and graphite are both partially due to the selection rules reducing the scattering rates of flexural phonon modes. These exact selection rules only strictly apply to perfectly two-dimensional materials; however, it may be possible to identify materials with the potential to be good thermal conductors based on their IFCs. For example, if the second-order IFCs result in a branch of phonon eigenvectors that are strictly perpendicular to the other branches eigenvectors, then the probability of scattering events involving phonons from that branch and the others may be significantly reduced, resulting in an enhanced thermal conductivity.

## Bibliography


[1]A. K. Geim, "Graphene: status and prospects", Science **324**, 1530–1534 (2009).

[2]D. L. Nika and A. A. Balandin, "Two-dimensional phonon transport in graphene", Journal of Physics: Condensed Matter **24**, 233203 (2012).

[3]A. B. Kaul, "Two-dimensional layered materials: structure, properties, and prospects for device applications", Journal of Materials Research **29**, 348–361 (2014).

[4]A. Jain and A. J. McGaughey, "Strongly anisotropic in-plane thermal transport in single-layer black phosphorene", Scientific Reports **5** (2015).

[5]D. L. Nika and A. A. Balandin, "Phonons and thermal transport in graphene and graphene-based materials", Reports on Progress in Physics **80**, 036502 (2017).

[6]A. I. Cocemasov, C. I. Isacova, and D. L. Nika, "Thermal transport in semiconductor nanostructures, graphene, and related two-dimensional materials", Chinese Physics B **27**, 056301 (2018).

[7]K. S. Novoselov, A. K. Geim, S. V. Morozov, D. Jiang, Y. Zhang, S. V. Dubonos, I. V. Grigorieva, and A. A. Firsov, "Electric field effect in atomically thin carbon films", Science **306**, 666–669 (2004).

[8]S. Ghosh, I. Calizo, D. Teweldebrhan, E. P. Pokatilov, D. L. Nika, A. A. Balandin, W. Bao, F. Miao, and C. N. Lau, "Extremely high thermal conductivity of graphene: prospects for thermal management applications in nanoelectronic circuits", Applied Physics Letters **92**, 151911 (2008).

[9]S. V. Morozov, K. S. Novoselov, M. I. Katsnelson, F. Schedin, D. C. Elias, J. A. Jaszczak, and A. K. Geim, "Giant intrinsic carrier mobilities in graphene and its bilayer", Phys. Rev. Lett. **100**, 016602 (2008).

[10]H. Jang, C. R. Ryder, J. D. Wood, M. C. Hersam, and D. G. Cahill, "3d anisotropic thermal conductivity of exfoliated rhenium disulfide", Advanced Materials **29**, 1700650 (2017).

[11]M. Rahman, K. Davey, and S.-Z. Qiao, "Advent of 2D rhenium disulfide ($ReS_2$): fundamentals to applications", Advanced Functional Materials **27**, 1606129 (2017).

[12]G. Giovannetti, P. A. Khomyakov, G. Brocks, P. J. Kelly, and J. van den Brink, "Substrate-induced band gap in graphene on hexagonal boron nitride: ab initio density functional calculations", Phys. Rev. B **76**, 073103 (2007).

[13]K. P. Loh, Q. Bao, G. Eda, and M. Chhowalla, "Graphene oxide as a chemically tunable platform for optical applications", Nature Chemistry **2**, 1015–1024 (2010).

[14]Q. H. Wang, K. Kalantar-Zadeh, A. Kis, J. N. Coleman, and M. S. Strano, "Electronics and optoelectronics of two-dimensional transition metal dichalcogenides", Nature Nanotechnology **7**, 699–712 (2012).

[15]M. Chhowalla, H. S. Shin, G. Eda, L.-J. Li, K. P. Loh, and H. Zhang, "The chemistry of two-dimensional layered transition metal dichalcogenide nanosheets", Nature Chemistry **5**, 263–275 (2013).

[16]D. Jariwala, V. K. Sangwan, L. J. Lauhon, T. J. Marks, and M. C. Hersam, "Emerging device applications for semiconducting two-dimensional transition metal dichalcogenides", ACS Nano **8**, PMID: 24476095, 1102–1120 (2014).

[17]S. Manzeli, D. Ovchinnikov, D. Pasquier, O. V. Yazyev, and A. Kis, "2d transition metal dichalcogenides", Nature Reviews Materials **2**, 17033 (2017).

[18]Z. Luo, J. Maassen, Y. Deng, Y. Du, R. P. Garrelts, M. S. Lundstrom, P. D. Ye, and X. Xu, "Anisotropic in-plane thermal conductivity observed in few-layer black phosphorus", Nature Communications **6**, 8572 (2015).

[19]X. Yao, Y. Wang, X. Lang, Y. Zhu, and Q. Jiang, "Thickness-dependent bandgap of transition metal dichalcogenides dominated by interlayer van der waals interaction", Physica E: Low-dimensional Systems and Nanostructures **109**, 11–16 (2019).

[20]C. Ho, R. Powell, and P. Liley, "Thermal conductivity of the elements: a comprehensive review", J. Phys. Chem. Ref. Data, Suppl., v. 3, no. 1, pp. 1-796 (1974).

[21]A. Molina-Sánchez and L. Wirtz, "Phonons in single-layer and few-layer $MoS_2$ and $WS_2$", Phys. Rev. B **84**, 155413 (2011).

[22]P. Giannozzi, S. Baroni, N. Bonini, M. Calandra, R. Car, C. Cavazzoni, and D. Ceresoli, "QUANTUM ESPRESSO: a modular and open-source software project for quantum simulations of materials", J. Phys.: Condens. Matter **21** (2009).

[23]A. Togo and I. Tanaka, "First principles phonon calculations in materials science", Scr. Mater. **108**, 1–5 (2015).

[24]W. Li, J. Carrete, N. A. Katcho, and N. Mingo, "ShengBTE: a solver of the Boltzmann transport equation for phonons", **185**, 1747–1758 (2014).

[25]L. Lindsay, D. A. Broido, and N. Mingo, "Flexural phonons and thermal transport in graphene", Phys. Rev. B **82**, 115427 (2010).

[26]J. H. Seol, I. Jo, A. L. Moore, L. Lindsay, Z. H. Aitken, M. T. Pettes, X. Li, Z. Yao, R. Huang, D. Broido, N. Mingo, R. S. Ruoff, and L. Shi, "Two-dimensional phonon transport in supported graphene", Science **328**, 213–216 (2010).

[27]L. Lindsay, D. A. Broido, and N. Mingo, "Flexural phonons and thermal transport in multilayer graphene and graphite", Phys. Rev. B **83**, 235428 (2011).

[28]S. Ghosh, W. Bao, D. L. Nika, S. Subrina, E. P. Pokatilov, C. N. Lau, and A. A. Balandin, "Dimensional crossover of thermal transport in few-layer graphene", Nature Materials **9**, 555–558 (2010).

[29]C. Kittel, *Introduction to solid state physics*, 8th ed. (Wiley, 2005).

[30]N. W. Ashcroft and N. D. Mermin, *Solid state physics* (Saunders College Publishing, 1976).

[31]K. Momma and F. Izumi, "*VESTA3* for three-dimensional visualization of crystal, volumetric and morphology data", Journal of Applied Crystallography **44**, 1272–1276 (2011).

[32]D. D. L. Chung, "Review graphite", Journal of Materials Science **37**, 1475–1489 (2002).

[33]J. M. Ziman, *Electrons and phonons: the theory of transport phenomena in solids* (Oxford at the Clarendon Press, 1960).

[34]M. Lundstrom, *Fundamentals of carrier transport*, 2nd ed. (Cambridge, 2000).

[35]R. Peierls, S. Rudolf Ernst Peierls, R. Peierls, and O. U. Press, *Quantum theory of solids*, International series of monographs on physics (Clarendon Press, 1955).

[36]M. Omini and A. Sparavigna, "An iterative approach to the phonon Boltzmann equation in the theory of thermal conductivity", Physica B: Condensed Matter **212**, 101–112 (1995).

[37]L. Lindsay and D. A. Broido, "Three-phonon phase space and lattice thermal conductivity in semiconductors", Journal of Physics: Condensed Matter **20**, 165209 (2008).

[38]P. Hohenberg and W. Kohn, "Inhomogeneous electron gas", Phys. Rev. **136**, B864–B871 (1964).

[39]W. Kohn and L. J. Sham, "Self-consistent equations including exchange and correlation effects", Phys. Rev. **140**, A1133–A1138 (1965).

[40]A. D. Becke, "Density-functional exchange-energy approximation with correct asymptotic behavior", Phys. Rev. A **38**, 3098–3100 (1988).

[41]S. Baroni, S. de Gironcoli, and A. D. Corso, "Phonons and related crystal properties from density-functional perturbation theory", Reviews of Modern Physics **73**, 516–557 (2001).

[42]P. E. Blöchl, "Projector augmented-wave method", Phys. Rev. B **50**, 17953–17979 (1994).

[43]J. P. Perdew, K. Burke, and M. Ernzerhof, "Generalized gradient approximation made simple", Phys. Rev. Lett. **77**, 3865–3868 (1996).

[44]A. D. Becke and E. R. Johnson, "Exchange-hole dipole moment and the dispersion interaction revisited", The Journal of Chemical Physics **127**, 154108 (2007).

[45]A. Otero-de-la-Roza and E. R. Johnson, "Van der Waals interactions in solids using the exchange-hole dipole moment model", The Journal of Chemical Physics **136**, 174109 (2012).

[46]J. Maultzsch, S. Reich, C. Thomsen, H. Requardt, and P. Ordejón, "Phonon dispersion in graphite", Phys. Rev. Lett. **92**, 075501 (2004).

[47]M. Mohr, J. Maultzsch, E. Dobardžić, S. Reich, I. Milo ševi ć, M. Damnjanovi ć, A. Bosak, M. Krisch, and C. Thomsen, "Phonon dispersion of graphite by inelastic x-ray scattering", Phys. Rev. B **76**, 035439 (2007).

[48]L. Wirtz and A. Rubio, "The phonon dispersion of graphite revisited", Solid State Communications **131**, 141–152 (2004).

[49]W. Cai, A. L. Moore, Y. Zhu, X. Li, S. Chen, L. Shi, and R. S. Ruoff, "Thermal transport in suspended and supported monolayer graphene grown by chemical vapor deposition", Nano Letters **10**, PMID: 20405895, 1645–1651 (2010).

[50]B. D. Kong, S. Paul, M. B. Nardelli, and K. W. Kim, "First-principles analysis of lattice thermal conductivity in monolayer and bilayer graphene", Phys. Rev. B **80**, 033406 (2009).

[51]G. Fugallo, A. Cepellotti, L. Paulatto, M. Lazzeri, N. Marzari, and F. Mauri, "Thermal conductivity of graphene and graphite: collective excitations and mean free paths", Nano Letters **14**, PMID: 25343716, 6109–6114 (2014).